Mohammad Miraskari[1]
Mechanical Engineering Department,
University of British Columbia,
2054-6250 Applied Science Lane,
Vancouver, BC V6T 1Z4, Canada
e-mail: m.miraskari@alumni.ubc.ca

Farzad Hemmati
Mechanical Engineering Department,
University of British Columbia,
2054-6250 Applied Science Lane,
Vancouver, BC V6T 1Z4, Canada
e-mail: farhemmati@alumni.ubc.ca

Alireza Jalali
Mechanical Engineering Department,
University of British Columbia,
2054-6250 Applied Science Lane,
Vancouver, BC V6T 1Z4, Canada
e-mail: arjalali@interchange.ubc.ca

M. Y. Alqaradawi
Department of Mechanical
and Industrial Engineering,
College of Engineering,
Qatar University,
P.O. Box 2713,
Doha, Qatar
e-mail: myq@qu.edu.qa

Mohamed S. Gadala
Mechanical Engineering Department,
University of British Columbia,
2054-6250 Applied Science Lane,
Vancouver, BC V6T 1Z4, Canada;
Department of Mechanical Engineering,
Abu Dhabi University,
Abu Dhabi, UAE
e-mail: gadala@mech.ubc.ca

A Robust Modification to the Universal Cavitation Algorithm in Journal Bearings

In the current study, a modified fast converging, mass-conserving, and robust algorithm is proposed for calculation of the pressure distribution of a cavitated axially grooved journal bearing based on the finite volume discretization of the Adams/Elrod cavitation model. The solution of cavitation problem is shown to strongly depend on the specific values chosen for the lubricant bulk modulus. It is shown how the new proposed scheme is capable of handling the stiff discrete numerical system for any chosen value of the lubricant bulk modulus (β) and hence a significant improvement in the robustness is achieved compared to traditionally implemented schemes in the literature. Enhanced robustness is shown not to affect the accuracy of the obtained results, and the convergence speed is also shown to be considerably faster than the widely used techniques in the literature. Effects of bulk modulus, static load, and mesh size are studied on numerical stability of the system by means of eigenvalue analysis of the coefficient matrix of the discrete numerical system. It is shown that the impact of static load and mesh size is negligible on numerical stability compared to dominant significance of varying bulk modulus values. Common softening techniques of artificial bulk modulus reduction is found to be tolerable with maximum two order of magnitudes reduction of β to avoid large errors of more than 3–40% in calculated results. [DOI: 10.1115/1.4034244]

Keywords: axially grooved journal bearings, cavitation algorithm, Adams/Elrod model, lubricant bulk modulus, numerical stability

1 Introduction

First successful mathematical model ever proposed for the lubrication problem was by Osborne Reynolds in 1886. Even Reynolds himself was doubtful that the fluid film can sustain subatmospheric pressures and hence he limited his analysis to lower eccentricities. The remarkable analytical solution to the Reynolds equation by Sommerfeld in 1904 predicted a negative antisymmetric pressure (tensile stress) in the divergent region of the bearing with magnitudes as large as the positive pressure one. Liquids in pure form or with small amount of dissolved gaseous content were reported to withstand tensile stresses of even up to hundreds of atmospheres [1]. However, in tribological environments with extreme shearing of the lubricant and high rates of heat generation and dissipation, a film rupture is expected when the fluid pressure drops below the saturation pressure of the dissolved gases (gaseous cavitation) or below the vapor pressure (vapor cavitation or boiling) [2]. The onset and extent of liquid cavitation in fluid film bearings is equally important in determining the load capacity of a fluid film bearing as well as largely influencing the rotor-dynamic stability of a rotor-bearing system and its maximum whirl amplitude of vibration [3]. Furthermore, vapor cavitation collapse (implosion) can cause severe surface material damage.

Regardless of the nature of the bubbles that form during cavitation, being caused by the environment or coming from the lubricant film itself, they induce a rupture in the continuous lubricant film. This happens in the diverging part of the lubricant film where the original Reynolds theory predicts negative pressures. Although the existence of the cavitated region is well understood, the exact position of the rupture interface and the applied boundary conditions at the interface are subjects of considerable discussion.

The first attempt in accounting for the film rupture was by Gumbel in 1914 by assuming the boundary of rupture originating in the immediate vicinity of the film minimum thickness and neglecting the subambient pressure loop completely when calculating bearing performance. His work falls short mainly in not respecting the mass continuity at the interface and not accounting for the film reformation. Although the pressure predictions based on the Gumbel condition is at variance with experimental data, it does give closed-form solution for bearing performance and is still employed in theoretical work [4]. The next major work came from Swift and Stieber in 1932 where they assumed a zero pressure gradient at the start of the cavitation zone. The algorithm proposed by Christopherson [5] in 1941 is based on the Swift–Stieber model and has been widely used in numerical analysis due to its ease of implementation. The main disadvantage of the

[1]Corresponding author.

Contributed by the Tribology Division of ASME for publication in the JOURNAL OF TRIBOLOGY. Manuscript received March 9, 2016; final manuscript received June 14, 2016; published online November 9, 2016. Assoc. Editor: Jordan Liu.

Christopherson algorithm is that it is not mass-conserving and it is not capable of presenting the subcavity pressures that occur just upstream from the cavitation boundary. Nonmass-conserving schemes are shown to predict incomplete identification of the film rupture and incorrect detection of the film reformation. Analysis of dynamic journal bearings and bearings with textured surfaces showed that ensuring the mass continuity is necessary for correct prediction of the film rupture and reformation [6,7].

Majority of the existing mass-conserving algorithms are based on the notable work of Jakobsson and Floberg [8] and Olsson [9], together known as JFO cavitation model, which assumes a constant pressure everywhere in the cavitation region ($P = P_{\mathrm{cav}}$) and hence taking the pressure gradient to be zero in the cavitated region. Their model also provides boundary conditions that conserve the mass at the interface between the full film (noncavitated) and the cavitation zones at rupture and reformation boundaries. The JFO model semi-accurately [10] predicts the onset and shape of the cavitation region in bearings that operate at moderate to high journal eccentricities (i.e., moderate to large static loads). The main disadvantage of the JFO model is the difficulty of implementation in computer codes due to complexity of numerical treatment of the nonlinear boundary conditions. Elrod and Adams [11,12] developed a finite difference algorithm based on the JFO theory but in a very simple manner. They introduced a change of variable that is related to the film pressure through the bulk modulus of the lubricant and rewrote the governing equations (in terms of the new variable) assuming constant bulk modulus throughout the lubricant film. They also combined two governing equations into a single equation throughout the lubrication region by proper use of a switch function to suppress the pressure driven terms in the cavitated region. Their ingenious approach was very successful for cavitated journal bearing performance predictions and is usually referred to as the universal cavitation algorithm. The cavitation algorithm was then mainly solved by means of Gauss–Seidel based relaxation methods [7,13] or alternate direction implicit (ADI) [3,14].

Vijayaraghavan and Keith [15] addressed a change of type of the partial differential equation (PDE) at the cavitation boundary and designed an algorithm that takes this change into consideration to further refine the computational efficiency. As relaxation and ADI methods require large computing times to convergence, different algorithms were proposed to enhance the convergence speed of the Elrod algorithm. Vijayaraghavan and Keith [15] proposed the use of approximate factorization (AF) technique. Woods and Brewe [16] and Qiu and Khonsari [17] advocated the use of multigrid techniques to accelerate the convergence speed.

The implementation of the universal cavitation algorithm is generally troubling in a computer code mainly due to dependency of the numerical efficiency on the chosen values for the lubricant bulk modulus (β). Choosing β values close to its physical value of approximately 2 GPa can render the system of equations too stiff for obtaining accurate solutions and it can also affect the convergence speed drastically. This difficulty was addressed by choosing artificially low values for β [11,15], claiming that this particular choice does not affect the final results [18]. Many subsequent studies showed that the choice of β indeed affect the performance predictions of the journal bearings [19–22].

Sahlin et al. [22] reported that treating the bulk modulus as a constant in the whole domain can produce accurate results only for a narrow pressure range. They introduced an algorithm mainly based on the Elrod algorithm but with an arbitrary choice for pressure-density to account for bulk modulus variations with pressure and noted the importance of the bulk modulus on the final calculations. Bayada and Chupin [20] and Bayada [23] proposed an algorithm similar to Elrod–Adams by directly solving the constitutive equations of the lubricant with detailed descriptions of the mixture characteristics in the cavitated region. They proposed a smooth pressure-density relation similar to Sahlin et al. [22] together with models for viscosity variations with density. Their unified treatment of the cavitated and full film regions eliminate the need for up-winding differencing in cavitation region and it naturally allows for subcavitation pressures in the cavitation region which is in-line with experimental predictions of pressures as low as 0.07 MPa upstream of the rupture interface [24]. Also, they showed how the choice of the lubricant bulk modulus can change the pressure distribution and the cavitation boundary; however, there was no reference on how this choice can affect the performance of the numerical scheme itself.

As an alternative approach to the universal cavitation algorithm, Giacopini et al. [25] proposed a mass-conserving linear complementarity formulation for the one-dimensional (1D) cavitation problem. The major advantage of their complementarity formulation is that it alleviates the problems associated with the need to change the scheme differencing method as a result of a change in the PDE type at the cavitation boundary. Bertocchi et al. [21] extended the original 1D linear complementarity problem (LCP) formulation of Giacopini et al. [25] to include the effects of fluid compressibility (pressure-density relationship), piezoviscosity (variation of viscosity with pressure), and non-Newtonian fluid behavior (shear rate dependence of lubricant viscosity) for 1D and two-dimensional (2D) cavitation problems. Almqvist et al. [19] proposed a model starting from the expression of the mass flow that leads directly to the linear complementarity problem (LCP). The linearity is guaranteed by treating β as a constant. They reported on the influence of chosen bulk modulus values (100 MPa up to 10 GPa) on fluid film pressure and suggested that the load carrying capacity of the bearing increases as the compressibility of the fluid decreases. The LCP based algorithms do offer benefits compared to the Switch function approaches; however, a complete performance analysis of these algorithms is missing in the literature, and hence, their computational efficiency is unclear and undocumented.

In this paper, the long lasting problem with robustness of the universal cavitation algorithm is addressed. Based on the finite volume discretization of the governing equations of motion, an alternative solution scheme is proposed as an attempt to accelerate the convergence speed of mass-conserved Elrod–Adams algorithm and eliminate the scheme dependency on chosen values of the lubricant bulk modulus. The resulting scheme shows very promising boost in robustness and convergence speed. The cost of artificially decreasing the bulk modulus on computed results is discussed and recommendations are given on the safe margin for such reduction to stabilize the scheme while maintaining the desired accuracy. The dependence of the scheme stability on various input parameters is systematically studied by means of a thorough eigenvalue analysis of the coefficient matrix of the discretized system of equations.

2 Mathematical Model for Mass Conserving Cavitation Problem

The Elrod Adams (E.A.) algorithm [11] with Vijayaraghavan and Keith [26] treatment is studied here as the underlying mathematical model. The standard J.F.O/E.A. treatment is based on acknowledging the fact that Poiseuille (pressure gradient) terms in the compressible Reynolds equation vanish in the cavitated region where the mass flow is only governed by the Couette (advective) terms. This distinction between the two regions of the flow will then lead to a mathematical model with two governing equations for full film and cavitated regions as [4]

$$\begin{aligned}\frac{\partial(\rho h)}{\partial t}+\frac{\partial}{\partial x}\left(\frac{\rho h U}{2}-\frac{\rho h^3}{12\mu}\frac{\partial p}{\partial x}\right)-\frac{\partial}{\partial z}\left(\frac{\rho h^3}{12\mu}\frac{\partial p}{\partial z}\right)=0\\ \frac{\partial(\rho h)}{\partial t}+\frac{\partial}{\partial x}\left(\frac{\rho h \mu}{2}\right)=0\end{aligned} \tag{1}$$

where ρ is the fluid density, h is the film thickness, $U = R\omega$ is the journal surface velocity, p is the fluid film pressure, and μ is the lubricant viscosity. Several pressure-density relations are proposed in the literature to relate the change of lubricant density to the lubricant pressure. In general, the validity of such relations is a function of induced pressures in the lubricant [27]. The pressure-density relation can be expressed in its most general form [21]

$$\rho = \rho_c f(p) \tag{2}$$

The most widely adopted compressibility relation in lubrication applications is based on constant bulk modulus (β) of the lubricant

$$\rho = \rho_c \ \exp\left(\frac{p - p_c}{\beta}\right) \tag{3}$$

where p_c and ρ_c are the pressure and density in the cavitated region. A generalization of Eq. (3) in the form of Eq. (2) can be easily adopted [19] in rewriting the compressible Reynolds equation but is omitted here for simplicity and the constant bulk modulus model is therefore used for the analysis in the present paper.

The J.F.O/E.A. mathematical model is mass converging and can also be derived directly from the continuity equation [19] assuming a homogeneous three-dimensional flow [23]. The major difficulty here is that although the governing equations for each region of the flow are simply stated, identifying the cavitation boundary separating the two regions can be troubling. The pioneering work of Elrod and Adams [11] suggested the use of a switch function, g, as well as a change of variable in an effort to unify the two governing equations into one equation

$$g = \begin{cases} 1, & \text{in full film region} \\ 0, & \text{in cavitated region} \end{cases} \qquad \alpha = \frac{\rho}{\rho_c} \tag{4}$$

where α is the density ratio. The switch function permits pressure terms to be retained in full film region or to be neglected in cavitation region. Equation (3) can be rewritten such that

$$p = p_c + g\beta \ \ln(\alpha) \tag{5}$$

The pressure is approximately uniform in the cavitated region and is equal to p_c. Since the typical lubricant bulk modulus β is a large number ($\cong$ 2 GPa), the density ratio (α) is only slightly greater than unity in the full film region, and hence, Eq. (5) can be approximately expressed in a simpler form [14]

$$p = p_c + g\beta \ (\alpha - 1) \tag{6}$$

Hence, the modified compressible Reynolds equation for the new variable α becomes [4]

$$\frac{\partial(\alpha h)}{\partial t} + \frac{\partial}{\partial x}\left(\frac{Uh\alpha}{2} - \frac{\beta h^3}{12\mu} g \frac{\partial \alpha}{\partial x}\right) - \frac{\partial}{\partial z}\left(\frac{\beta h^3}{12\mu} g \frac{\partial \alpha}{\partial z}\right) = 0 \tag{7}$$

The solution to Eq. (7) will yield the density ratio, α. The induced pressure then is easily found through Eq. (6). In order to solve Eq. (7), a finite volume discretization is employed here.

3 Numerical Treatment of Cavitation Based on a Finite Volume Method (FVM)

3.1 Discretization. Nondimensionalizing the governing PDE of Eq. (7) is preferred for versatility of the numerical analysis and faster convergence. The nondimensionalized variables are as follows:

$$\bar{x} = \frac{x}{2\pi R}, \quad \bar{z} = \frac{z}{L}, \quad H = \frac{h}{C}, \quad \bar{\beta} = \frac{\beta}{\mu\omega}\left(\frac{C}{R}\right)^2, \quad \bar{t} = \omega t \tag{8}$$

where R, L, C, and ω are journal radius, length, clearance, and rotational velocity, respectively. By substituting the nondimensional variables of Eq. (8) back into Eq. (7), the nondimensional form can be constructed as

$$\frac{\partial(\alpha H)}{\partial \bar{t}} + \frac{\partial}{\partial \bar{x}}\left(\frac{\alpha H}{4\pi} - \frac{\bar{\beta}}{48\pi^2} H^3 g \frac{\partial \alpha}{\partial \bar{x}}\right) - \frac{\partial}{\partial \bar{z}}\left(\frac{\bar{\beta}}{48(L/D)^2} H^3 g \frac{\partial \alpha}{\partial \bar{z}}\right) = 0 \tag{9}$$

Inclusion of the switch function in Eq. (9) requires some attention. Similar to the treatment in Ref. [14], the pressure induced flow term can be re-arranged such that

$$g\frac{\partial \alpha}{\partial \bar{x}} = g\frac{\partial(\alpha - 1)}{\partial \bar{x}} = \frac{\partial g(\alpha - 1)}{\partial \bar{x}} - (\alpha - 1)\frac{\partial g}{\partial \bar{x}} \tag{10}$$

The term $(\alpha - 1)\partial g/\partial \bar{x}$ vanishes for any α since the switch function, g only changes at $\alpha = 1$. Hence

$$g\frac{\partial \alpha}{\partial \bar{x}} = \frac{\partial g(\alpha - 1)}{\partial \bar{x}} \tag{11}$$

Similar treatment for the other pressure driven term will simplify Eq. (9) to

$$\frac{\partial(\alpha H)}{\partial \bar{t}} + \frac{\partial}{\partial \bar{x}}\left(\frac{\alpha H}{4\pi} - \frac{\bar{\beta}}{48\pi^2} H^3 \frac{\partial g(\alpha - 1)}{\partial \bar{x}}\right) - \frac{\partial}{\partial \bar{z}}\left(\frac{\bar{\beta}}{48(L/D)^2} H^3 \frac{\partial g(\alpha - 1)}{\partial \bar{z}}\right) = 0 \tag{12}$$

Representing Eq. (12) in a general form suitable for discretization and dropping all the nondimensional bars for simplifying notation, we can write

$$\frac{\partial u}{\partial t} + \frac{\partial F}{\partial x} + \frac{\partial G}{\partial z} = 0 \tag{13}$$

where

$$u = \alpha H \qquad F = \frac{\alpha H}{4\pi} - \frac{\beta}{48\pi^2} H^3 \frac{\partial g(\alpha - 1)}{\partial x} \qquad G = \frac{\beta}{48(L/D)^2} H^3 \frac{\partial g(\alpha - 1)}{\partial z} \tag{14}$$

A finite volume discretization technique is applied for solving Eq. (13). Taking the control volume integral (in this case a control surface) of Eq. (13) over the volume (surface) of a two-dimensional representative cell with area of $\Delta x \ \Delta z$ will yield

$$\iint \frac{\partial u}{\partial t} dA + \iint \left(\frac{\partial F}{\partial x} + \frac{\partial G}{\partial z}\right) dA = 0 \tag{15}$$

Applying the Gauss's theorem in plane and assuming a fixed control surface with no moving boundaries and defining $\mathbf{F} = F\ \hat{i} + G\ \hat{k}$ will result in

$$\frac{d}{dt}\iint u \ dA + \oint \mathbf{F} \cdot n \ dS = 0 \tag{16}$$

Defining the control surface average quantity as

$$\bar{u}_{i,j} = \frac{1}{A_{i,j}}\iint u\ dA = \frac{1}{\Delta x\ \Delta z}\iint u\,dx\ dz \tag{17}$$

and performing the contour integral over the boundary of the representative 2D cell for the last two terms in Eq. (16) will yield

$$\frac{d\bar{u}_i}{d\bar{t}} + \frac{F_{i+\frac{1}{2},j} - F_{i-\frac{1}{2},j}}{\Delta x} + \frac{G_{i,j+\frac{1}{2}} - G_{i,j-\frac{1}{2}}}{\Delta z} = 0 \tag{18}$$

where the $1/2$ indices correspond to the value of the flux at the cell boundary as compared to the flux values at the cell center. In order to discretize the time dependent term, a first-order Implicit Euler method is adopted here. Hence, Eq. (18) can be written as

$$\frac{\bar{u}_{i,j}{}^{n+1} - \bar{u}_{i,j}{}^{n}}{\Delta t} + \frac{F_{i+\frac{1}{2},j}{}^{n+1} - F_{i-\frac{1}{2},j}{}^{n+1}}{\Delta x} + \frac{G_{i,j+\frac{1}{2}}{}^{n+1} - G_{i,j-\frac{1}{2}}{}^{n+1}}{\Delta z} = 0 \tag{19}$$

where superscript n indicates a variable value at the current time-step and superscript $n+1$ is to represent a variable value at the next time-step. Common to the implicit schemes, the variable value in the next time-step needs to be expressed in terms of the variable and its gradients at the current time-step by means of a Taylor series expansion of the fluxes

$$\begin{aligned} F_{i+\frac{1}{2},j}{}^{n+1} &= F_{i+\frac{1}{2},j}\left(\bar{u}_{i,j}{}^{n+1}\ ,\bar{u}_{i+1,j}{}^{n+1}\right) \\ &= F_{i+\frac{1}{2},j}\left(\bar{u}_{i,j}{}^{n} + \delta\bar{u}_{i,j}\ ,\ \bar{u}_{i+1,j}{}^{n} + \delta\bar{u}_{i+1,j}\right) \\ &= F_{i+\frac{1}{2},j}\Big|^{n} + \frac{\partial F_{i+\frac{1}{2},j}}{\partial \bar{u}_{i,j}}\Big|^{n}\delta\bar{u}_{i,j} + \frac{\partial F_{i+\frac{1}{2},j}}{\partial \bar{u}_{i+1,j}}\Big|^{n}\delta\bar{u}_{i+1,j} + O(\delta\bar{u}^2) \end{aligned} \tag{20}$$

where $\delta\bar{u}_{i,j} = \bar{u}_{i,j}{}^{n+1} - \bar{u}_{i,j}{}^{n}$ and $F_{i+\frac{1}{2},j}\big|^{n} = F_{i+\frac{1}{2},j}(\bar{u}_{i,j}{}^{n}\ ,\bar{u}_{i+1,j}{}^{n})$. Other terms in Eq. (19) are treated in a similar fashion. Plugging zero- and first-order Taylor expand terms back into Eq. (19) will result in

$$\begin{aligned} &\delta\bar{u}_{i,j}\left(\frac{1}{\Delta t} + \frac{1}{\Delta x}\frac{\partial F_{i+\frac{1}{2},j}}{\partial \bar{u}_{i,j}}\Big|^{n} - \frac{1}{\Delta x}\frac{\partial F_{i-\frac{1}{2},j}}{\partial \bar{u}_{i,j}}\Big|^{n} + \frac{1}{\Delta z}\frac{\partial G_{i,j+\frac{1}{2}}}{\partial \bar{u}_{i,j}}\Big|^{n}\right. \\ &\left.-\frac{1}{\Delta z}\frac{\partial G_{i,j-\frac{1}{2}}}{\partial \bar{u}_{i,j}}\Big|^{n}\right) + \frac{1}{\Delta x}\frac{\partial F_{i+\frac{1}{2},j}}{\partial \bar{u}_{i+1,j}}\Big|^{n}\delta\bar{u}_{i+1,j} - \frac{1}{\Delta x}\frac{\partial F_{i-\frac{1}{2},j}}{\partial \bar{u}_{i-1,j}}\Big|^{n} \\ &\delta\bar{u}_{i-1,j} + \frac{1}{\Delta z}\frac{\partial G_{i,j+\frac{1}{2}}}{\partial \bar{u}_{i,j+1}}\Big|^{n}\delta\bar{u}_{i,j+1} - \frac{1}{\Delta z}\frac{\partial G_{i,j-\frac{1}{2}}}{\partial \bar{u}_{i,j-1}}\Big|^{n}\delta\bar{u}_{i,j-1} = FI^n \end{aligned} \tag{21}$$

where

$$FI^n = -\frac{F_{i+\frac{1}{2},j}{}^{n} - F_{i-\frac{1}{2},j}{}^{n}}{\Delta x} - \frac{G_{i,j+\frac{1}{2}}{}^{n} - G_{i,j-\frac{1}{2}}{}^{n}}{\Delta z}$$

is the flux integral that is evaluated at the nth time-step.

As noted by Vijayaraghavan and Keith [15,26], Eq. (9) has different characteristics in the full film and cavitation regions; being an elliptic PDE (similar to the Laplace equation) in the full film region and a hyperbolic PDE (similar to wave equation) in the cavitated region. Since the nature of the governing equation in the full film region is elliptic, the solution is expected to be smooth and hence central differencing schemes are desirable in this region. On the other hand, the hyperbolic nature of the PDE in the cavitated region necessitates the use of upwind flux functions to capture discontinuities and sudden changes in the flow field.

Vijayaraghavan and Keith [15,26] proposed adding higher-order artificial viscosity terms to the shear term in Eq. (9) in such a way that pressure induced flow terms exist in the full film region but vanish in the cavitated region. The whole equation can now be centrally differenced such that by substituting $g=1$ in the full film region, the central differencing remains in effect; and in the cavitation region central differencing automatically switches to second-order upwind differencing by substituting $g=0$ [15]. The shear term is then approximately expressed as

$$\frac{\partial u}{\partial x} = \frac{\partial}{\partial x}\left[u - (1-g)\left(\frac{\partial^2 u}{\partial x^2}\ \frac{\Delta x^2}{3} - \frac{\partial^3 u}{\partial x^3}\ \frac{\Delta x^3}{4}\right)\right] \tag{22}$$

By adding the artificial viscosity terms of Eq. (22), the fluxes in Eq. (14) are to be updated such that

$$\begin{aligned} u &= \alpha H \\ F &= \frac{u}{4\pi} - \frac{\beta}{48\pi^2}\ H^3\frac{\partial g(\alpha-1)}{\partial x} - \frac{(1-g)}{4\pi}\left(\frac{\partial^2 u}{\partial x^2}\ \frac{\Delta x^2}{3} - \frac{\partial^3 u}{\partial x^3}\ \frac{\Delta x^3}{4}\right) \\ G &= \frac{\beta}{48(L/D)^2}H^3\frac{\partial g(\alpha-1)}{\partial z} \end{aligned} \tag{23}$$

Substituting Eq. (23) into Eq. (21) will yield the discretized form of the governing PDE for the cavitation problem. Details of the substitution and the final discretized equation are given in the Appendix.

3.2 Solution Procedure. The discretized equation as detailed in the Appendix is shown to take the final form of

$$\begin{aligned} \text{LHS} = X_{-2}\ \delta u_{i-2,j} + X_{-1}\ \delta u_{i-1,j} + XZ_0\ \delta u_{i,j} \\ + X_{+1}\ \delta u_{i+1,j} + Z_{-1}\ \delta u_{i,j-1} + Z_{+1}\ \delta u_{i,j+1} \end{aligned} \tag{24}$$

The set of linear algebraic equations arisen form the discretized Reynolds equation has been solved in the literature with a variety of different methods such as conventional explicit successive over relaxation (SOR) scheme [7,13], implicit successive line over relaxation (SLOR), alternate direction implicit (ADI) [3,14], Multigrid SOR [16,17], and approximate factorization (AF) technique [15,26]. Linear systems arisen from implicit time schemes of the Adams/Elrod algorithm have commonly been solved using the approximate factorization technique [15,26,28,29].

Equation (24) is a single equation written for a representative cell for which its value depends on its immediate neighbors. By solving Eq. (24), the change in solution of the representative cell $\delta u_{i,j}$ at each time-step can be found. Writing Eq. (24) for all control volumes in the field gives a linear system of equations which takes the form of

$$(I + \Delta t\ D_x + \Delta t\ D_z)\delta\mathbf{U} = \mathbf{FI} \tag{25}$$

Assuming a n by m mesh, $\delta\mathbf{U}$ and FI are column vectors of size $n\times m$. I, D_x, D_y are square matrices with $n\times m$ rows and $n\times m$ columns. The underlying assumption in the approximate factorization technique is that the left-hand side (LHS) of Eq. (25) can be approximated by

$$(I + \Delta t\ D_x + \Delta t\ D_z) = (I + \Delta t\ D_x)(I + \Delta t\ D_z) \tag{26}$$

An extra term $\Delta t^2\ D_x\ D_z$ is added to the LHS of Eq. (25) as a result of the assumption as in Eq. (26). For time accurate solutions, this induced error is tolerable due to the fact that the space discretization was chosen to be second-order accurate for both full film and cavitation regions. However, if a higher-order space discretization scheme is needed, such approximation will force the whole scheme to be only second-order accurate. Hence, for any higher-order space discretization, the AF technique cannot be implemented unless the interest is only in finding the steady-state solution.

The major benefit from the AF technique is its ability to decouple the two physical dimensions such that the solution can be sought in x and z directions in a two-step process

$$(I+\Delta t\ D_x)\delta\tilde{U}=\mathbf{FI}$$
$$(I+\Delta t\ D_z)\delta\mathbf{U}=\delta\tilde{U} \tag{27}$$

where $\tilde{U}$ is the axillary solution vector. The tridiagonal linear systems of Eq. (27) can be solved on the domain, row by row and column by column, such that the size of coefficient matrices D_x and D_z can be significantly reduced from a full matrix of $n\times m$ by $n\times m$ for the whole domain to just $m\times m$ and $n\times n$, respectively. Such reduction can be beneficial wherever computer memory is of concern, but it does not significantly affect the overall computational cost since each linear system of reduced size needs to be repeatedly solved for every row and every column. As an alternative to the existing solution schemes and to enhance the robustness of the solver, a new scheme is proposed in this study.

3.3 Proposed Iterative Solver. The proposed scheme is mainly consists of three modifications to the currently existing and widely used Elrod/Adams algorithm with Vijayaraghavan and Keith treatment [11,12,15] such that:

(1) The system of linear equations is directly solved via Gaussian elimination in a single step for the full linear system (FLS) of Eq. (24) as shown in the Appendix. Solving the full system as compared to the approximate factorization based schemes has two immediate benefits: First, the low frequency error is attenuated much more effectively at each iteration and hence considerably fewer iterations are required for convergence. Second, it does not introduce an artificial error of second-order to the discretization and hence can be used for implicit time-accurate simulations. The scheme that is based on the direct solve of the full linear system of Eq. (24) will be referred to as FLS in this paper. It shall be noted that since in majority of lubrication problems the total number of elements is fairly limited, obtaining the exact solution to the discretized system is efficiently possible and hence implementation of iterative solvers for the linear system is not justified for the lubrication problem.

(2) The automatic time stepping method used here is based on an effective optimization scheme recently proposed by Ceze and Fidkowski [30] for aerodynamic problems. The update to the time-step size and the solution update at each iteration essentially will depend on an under-relaxation parameter ω such that

$$\mathbf{U}^{n+1}=\mathbf{U}^n+\omega_r\ \delta\mathbf{U} \tag{28}$$

The updated time-step magnitude is also a function of the under-relaxation parameter

$$\Delta t^{n+1}=\begin{cases}\gamma\ \Delta t^n, & \omega_r=1\\ \Delta t^n, & 0.01\le\omega_r\le 1\\ k\ \Delta t^n, & \omega_r<0.01\end{cases} \tag{29}$$

where ω_r is the under-relaxation parameter, and k and γ are tunable parameters with default values of 0.1 and 2, respectively. Defining the L_2 norm of the residual $R(U)$ as

$$\|R(U)\|_2=\sqrt{\frac{\sum_i\sum_j R(U)_{ij}{}^2}{i_{\max}\ j_{\max}}}=\sqrt{\frac{\sum_i\sum_j FI_{ij}{}^2}{i_{\max}\ j_{\max}}} \tag{30}$$

Note that the flux integral is a function of the available solution at the current time-step: $FI=FI(U^n)$. Algorithm 1 shows the steps for estimating the value of the under-relaxation parameter ω_r:

Algorithm 1

$\omega_r=1$
$\tilde{U}=\mathbf{U}^n+\omega_r\ \delta\mathbf{U}$
while $\left\|\frac{\tilde{U}-\mathbf{U}^n}{\Delta t}-R(\tilde{U})\right\|_2>\|R(U)\|_2$
$\omega_r=\dfrac{\omega_r}{2}$
$\tilde{U}=\mathbf{U}^n+\omega_r\ \delta\mathbf{U}$
end

Note that a line search algorithm is incorporated with the implicit solver to guarantee the reduction of residual norm in the next nonlinear iteration.

(3) The switch function is implemented based on the improved scheme of Fesanghary and Khonsari [31] such that while iterating, the switch function exponentially decays toward zero in cavitation region and exponentially grows toward unity in the full film region unlike the binary switching in the Elrod algorithm. The implementation is shown in Algorithm 2.

Algorithm 2

If $\alpha_{ij}\ge 1$
If gFactor >0
$g_{ij}=\dfrac{g_{ij}}{g\text{Factor}}$
else
$g_{ij}=1$
end
else
$g_{ij}=g_{ij}\times g$Factor
end

where gFactor is switch function multiplier with reported optimal value of 0.8 in Ref. [31].

4 Numerical Results

The proposed numerical scheme of Sec. 3.3 is compared to the traditional scheme based on the approximate factorization as implemented in Refs. [15], [26], [28], and [29]. Equation (A10) is solved over a structured mesh on the surface of a journal bearing as shown in Fig. 1(*a*). The computational domain is depicted in Fig. 1(*b*). The performance study of the scheme is categorized based on the solver type (AF or Full) and selected bulk modulus value (artificially softened or physical).

In order to show the performance in each case, three scheme indicators are studied. First, the evolution of the L_2 norm of the residual $\|R(U)\|_2$ as defined in Eq. (30) versus number of iterations is reported. The last two scheme indicators are the maximum pressure in the field and the Sommerfeld number (an average quantity) defined as

$$S=\frac{\mu\ N\ L\ D}{W}\left(\frac{R}{C}\right)^2 \tag{31}$$

where $N=\omega/2\pi$ and W is the bearing load capacity defined as

$$W=\int_0^{\theta_{\text{cav}}}\int_{-\frac{L}{2}}^{\frac{L}{2}}p\ R\ d\theta dz \tag{32}$$

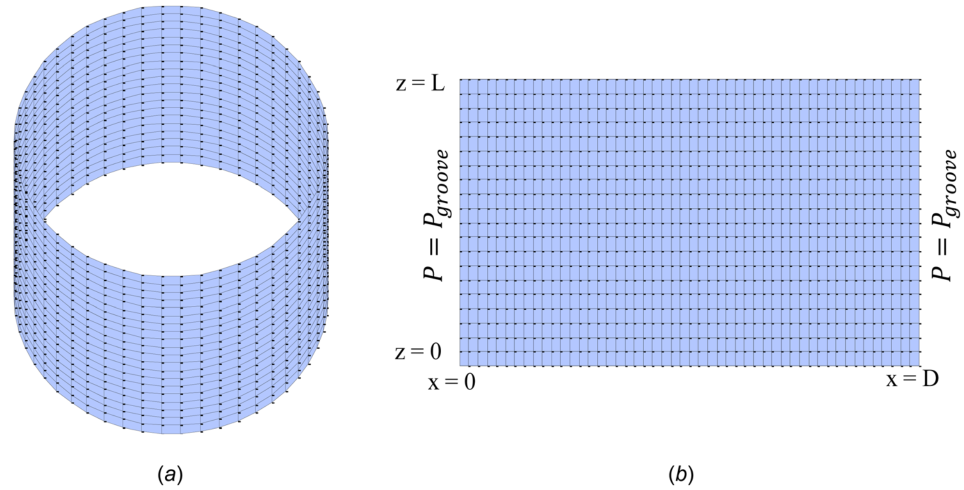

Fig. 1 Structured 50×20 mesh (*a*) and the computational domain (*b*)

Although predictions of the cavitation algorithm depend on the magnitudes of the lubricant bulk modulus (β) chosen for the analysis, realistic β magnitudes leads to a very stiff system of equations for which obtaining an accurate solution in a short period of time is considerably difficult. To avoid the accuracy and slow convergence issues, it is customary to choose artificially lower values for the bulk modulus in an attempt to soften the system of equations. Numerically stable algorithms have been proposed and shown to give acceptable results for β values of 1/100 to 1/10 of the more realistic values of $\beta \approx 2$ GPa [11,28,31]. An ideal scheme is therefore a scheme that can achieve accurate results in a relatively fast manner while the magnitude of the bulk modulus is as close as possible to the realistic physical values. To show the superiority of the numerical scheme proposed in Sec. 3.3, the performance prediction is carried out for the artificially softened and realistic system of equations as follows. All problems were solved with a personal computer on a single core of an Intel i7 chip at 3.40 GHz and 12 GB memory.

4.1 The Softened System of Equations. The boundary condition used for this analysis is the Dirichlet boundary condition for both circumferential (x) and longitudinal (z) directions as was shown in the computational domain in Fig. 1(*b*). The axial Dirichlet Boundary condition is based on selecting a grooved journal bearing with the groove located at the maximum film thickness. If the supplied oil pressure at the groove is equal to the cavitation pressure P_{cav}, reformation happens at the groove itself and there will be no reformation boundary to capture. This is the simplest case for the numerical scheme and is initially selected here. The scheme performance indicators for the softened system of equations at the reduced bulk modulus of $\beta = 20$ MPa ($\equiv \bar{\beta} = 2.75 \times 10^2$) is shown in Fig. 2(*a*) for AF and Fig. 2(*b*) for the FLS representation.

By direct comparison of the L_2 norm of the residual $R(U)_2$ for AF scheme in Fig. 2(*a*) and for the FLS scheme in Fig. 2(*b*), it can be seen that both schemes do converge and reach the preset goal of $\|R(U)\|_2 \leq 10^{-8}$. However, the number of required iterations to reach convergence is considerably lower for the full system; being 2676 for AF versus only 82 iterations for the FLS. As the computation cost per iteration is similar between the two schemes, fewer iterations required for reaching convergence in the FLS scheme also means faster convergence in computation time. To show similarity of computational cost per iteration, central

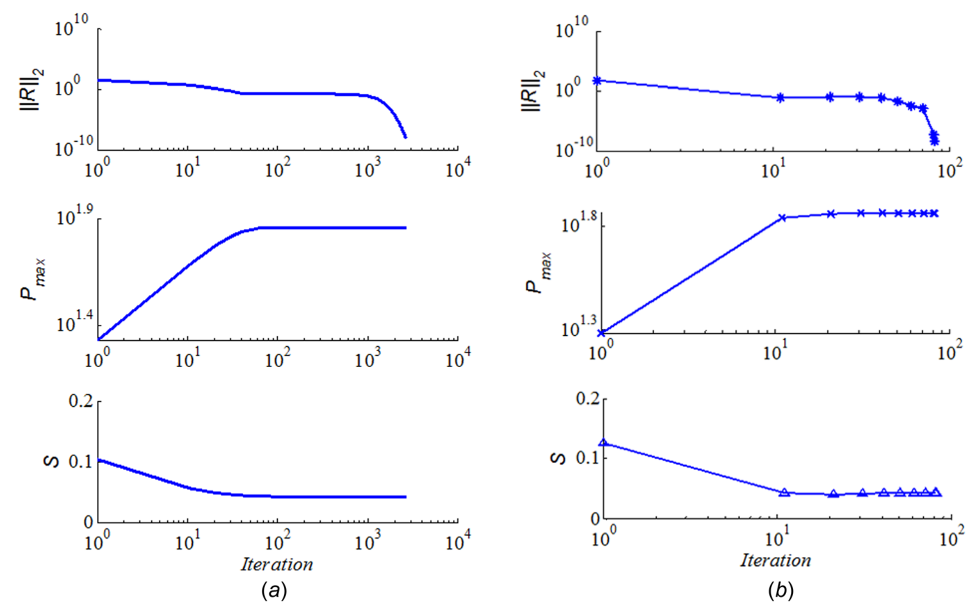

Fig. 2 Performance study of the softened system of equations at $\beta = 20$ MPa for the AF solver (*a*) and the FLS solver (*b*)

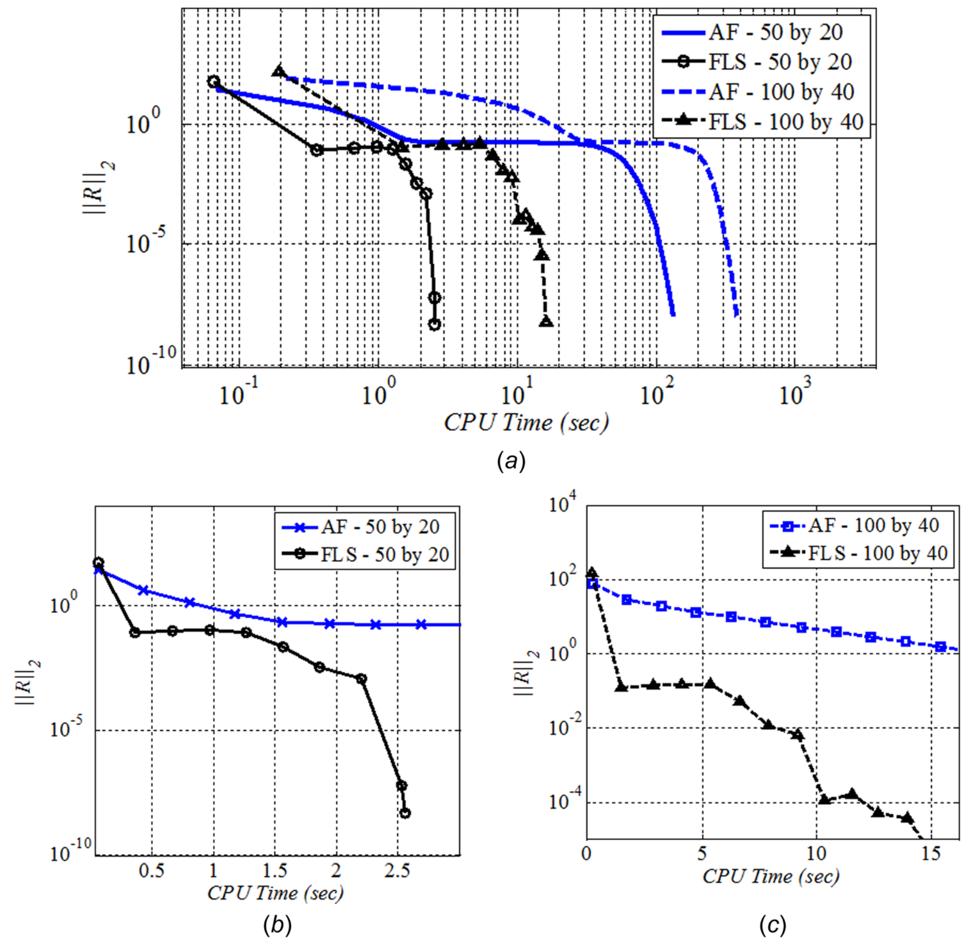

Fig. 3 CPU computation time of AF and FLS schemes for a 50 × 20 and a 100 × 40 mesh, total iterations to converge (*a*), first 100 iterations for 50 × 20 mesh (*b*), and first 120 iterations for 100 × 40 mesh (*c*)

processing unit (CPU) computation time of both schemes for two selected mesh sizes are compared to each other in Fig. 3.

Solution indicators for both schemes reaches the values of $\bar{P}_{\max} = 72.93$ and $S = 0.0427$ for a predefined eccentricity ratio of $\epsilon = 0.8$. In order to study what proportion in computation time and iterations is due to the effect of the full linear system representation versus approximate factorization, AF and FLS schemes were compared based on two different cases. "Case 1" with traditional binary switching of the switch function and with constant time-step and "Case 2" with all the features of the proposed algorithm as outlined in Sec. 3.3. Convergence plots for both cases versus iterations and CPU time is given in Figs. 4(*a*) and 4(*b*), respectively. It is noteworthy to mention that due to the superior robustness of the FLS based algorithm, the fixed time-step value chosen to perform the time marching can be chosen more than two to three orders of magnitude higher than the biggest time-step for which AF scheme remains numerically stable. Such an advantage will then result in much faster convergence as can be seen in Figs. 4(*a*) and 4(*b*).

4.2 The Stiff System of Equations. Performance studies for the system of equations with realistic bulk modulus values of $\beta = 2$ GPa ($\equiv \bar{\beta} = 2.75 \times 10^4$) are shown in Fig. 5.

The AF based method in solving the stiff system shows poor performance as can be marked by lack of convergence in Fig. 5(*a*). The lowest obtained value for $\|R(U)\|_2$ after 10,000 iterations is only 0.018 and hence the predefined goal of 10^{-8} is not achieved. On the contrary, the FLS scheme converges in just 145 iterations, only a few iterations more than what was required for the softened system. The final obtained values for nondimensional maximum pressure are $\bar{P}_{\max} = 70.18$ and $\bar{P}_{\max} = 70.21$ for the AF and Full schemes, respectively. The distribution of error in obtaining the nondimensional pressure ($d\bar{P} = \bar{P}|_{\mathrm{FLS},\beta=2\ \mathrm{GPa}} - \bar{P}|_{\mathrm{AF},\beta=2\,\mathrm{GPa}}$) over the whole domain is shown in Fig. 6(*a*). The error was found to accumulate close to and downstream of the cavitation boundary where there is a switch in the differencing scheme from central to upwind.

It is expected that if the norm of the residuals reaches the predefined goal, the discrepancy between the calculated pressure values vanishes. However, this is not computationally effective since the number of iterations required for such reduction in residual norms is far more than what is needed for the FLS based scheme and hence its superiority in solving the stiff system of equations is evident. The L_2 norm of the residual of both schemes is superimposed for both the softened and the rigid numerical systems versus iterations and is shown against iteration number in Fig. 6(*b*).

4.3 Verification and Comparison of Results. A mesh sensitivity analysis is carried out for the nonpressurized axially grooved bearing at $\beta = 2\,\mathrm{GPa}$ and $\epsilon = 0.8$ in both x and z directions separately and are shown in Fig. 7. The maximum field pressure as well as the Sommerfeld number and cavitation location at journal centerline along x-axis are selected as target variables (φ) of interest for mesh sensitivity analysis.

As can be seen in Fig. 7, the evolution of solution parameters with increasing mesh-size in both Z and X directions becomes insignificant after 40 and 100 divisions, respectively. To study the

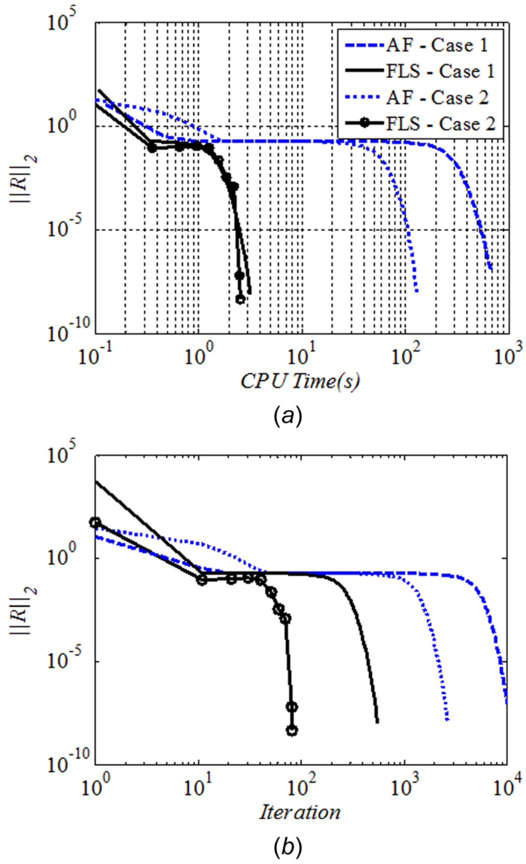

Fig. 4 Performance study (*a*) and CPU computation time (*b*) of the softened system of equations at $\beta = 20$ MPa for AF and FLS schemes with binary switch function and fixed time-step

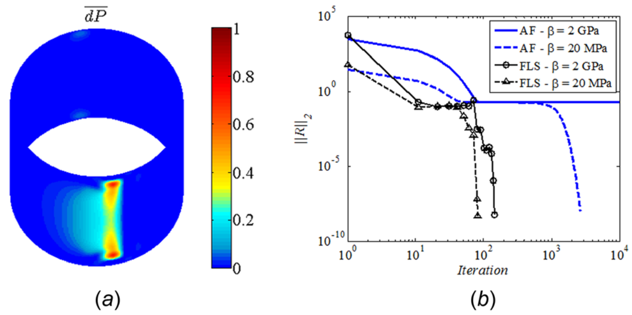

Fig. 6 Error distribution dP (*a*) and L_2 norms of the residual (*R*2) versus iterations for rigid and softened system based on AF and FLS schemes (*b*)

effect of increasing mesh-size in both directions simultaneously with estimated uncertainties in obtaining the solution, the fine grid convergence index GCI_{fine}[21] (an indicator of numerical uncertainty in obtaining the solution for a particular mesh) as well as extrapolated target variables Φ_{ext} and corresponding grid error for a selected mesh (50×20, 100×40, and 200×80) are calculated based on Ref. [32] and are tabulated in Table 1.

As shown in Table 1, the coarse grid (50×20 (x, z)) and intermediate grid (100×40) convergence indices $\%GCI_{coarse}$[32] and $\%GCI_{fine}$[21], indicating numerical uncertainty in calculating maximum target variables in the coarsest and intermediate grids, do not exceed %1.2 and %0.6 for any of the calculated solution indicators of both grids, respectively. Hence, both the coarsest and intermediate grids are acceptable and the coarse grid is used in this paper for scheme performance analysis.

4.3.1 Comparisons and Verification. Case 1-1: Pure Sliding Motion Without Reformation

In this case, the 1D problem of a hydrodynamic bearing with a convergent–divergent sinusoidal profile as shown in Fig. 8 is studied.

This particular example is chosen identical to those of Giacopini et al. [25] for comparison of the current proposed algorithm to the LCP-based type algorithms of Refs. [19], [21], and [25]. The selected parameters are tabulated in Table 2. The external pressures are chosen as $P_0 = P_a = 0$, and hence, no film reformation occurs. The pressure curve is calculated by the FLS algorithm at a remarkably high bulk modulus of $\beta = 100$ GPa (to mimic incompressibility) on a uniform mesh of 60 elements and is

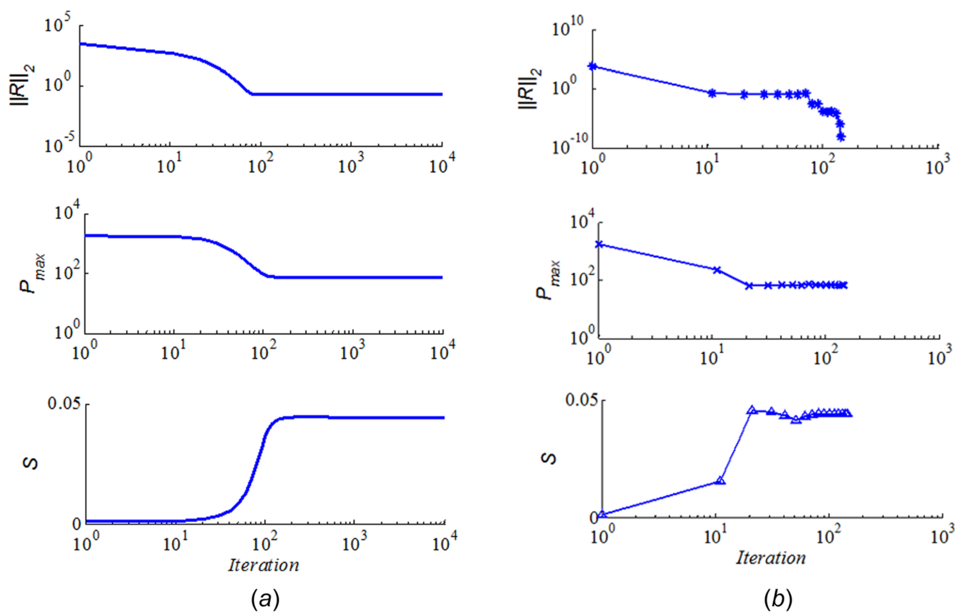

Fig. 5 Performance study of the stiff system of equations at $\beta = 2$ GPa for the AF solver (*a*) and the full linear system solver (*b*)

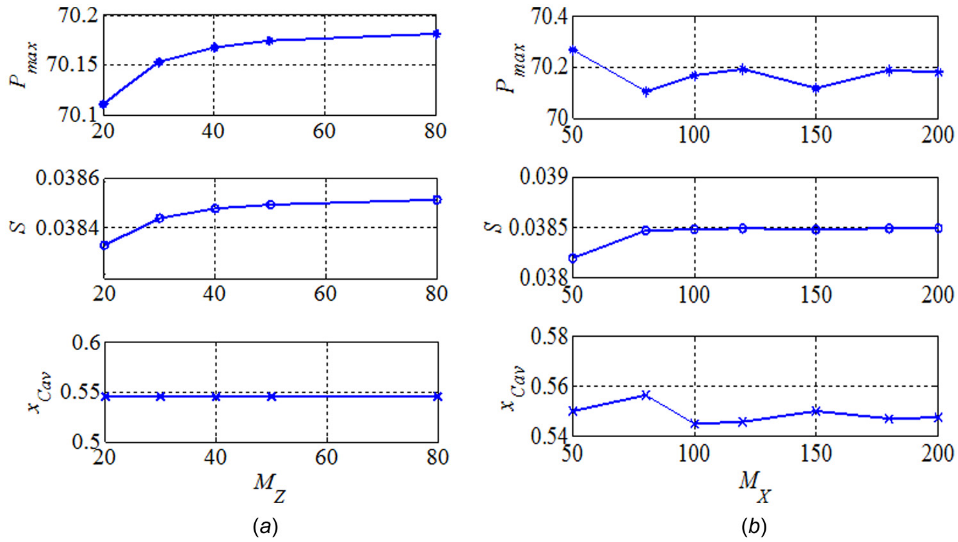

Fig. 7 Mesh-sensitivity analysis in Z (a) and X (b) directions

Table 1 Sample calculations of discretization errors

	$\Phi = P_{\max}$	$\Phi = S$	$\Phi = \bar{x}_{\mathrm{cav}}$
Φ_1 (fine grid)	70.1928	0.0385	0.5475
Φ_2	70.1674	0.0385	0.5450
Φ_3 (coarse grid)	70.2087	0.0380	0.5500
Φ_{ext}^{32}	70.1012	0.0385	0.5400
Φ_{ext}^{21}	70.2336	0.0385	0.5500
$\%e_{\mathrm{ext}}^{32}$	0.0944	0.1332	0.9259
$\%e_{\mathrm{ext}}^{21}$	0.0581	0.0139	0.4545
$\%\mathrm{GCI}_{\mathrm{coarse}}^{32}$	0.1179	0.1667	1.1468
$\%\mathrm{GCI}_{\mathrm{fine}}^{21}$	0.0726	0.0174	0.5708

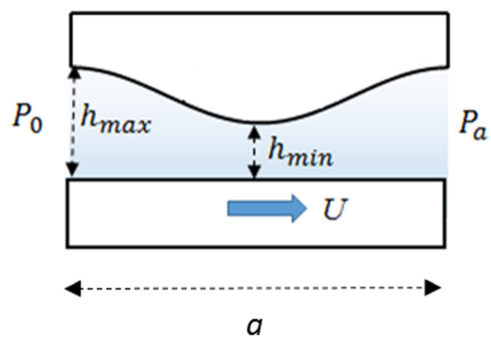

Fig. 8 Schematic of a convergent–divergent bearing under pure sliding motion as in Ref. [25]

compared to the incompressible solution of Giacopini et al. [25] in Fig. 9(a).

Case 1-2: Pure sliding motion with reformation

If the external pressures are chosen as $P_0 = P_a = 1$ MPa, reformation takes place in the lubricated film. The obtained pressure distribution is calculated and compared to that of Ref. [25] and is shown in Fig. 9(b).

Pressure distributions obtained by the FLS algorithm agrees with the results of Giacopini et al. [25] with and without reformation as depicted in Fig. 9. This agreement was indeed expected as both algorithms are mass conserving.

Case 2-1: Axially grooved journal bearing with nonpressured groove (no reformation)

Comparison of the scheme indicators as well as the predicted solution indicators of a nonpressured grooved journal bearing ($\bar{P}_g = 0$) for a range of lubricant bulk modulus is given in Table 3 at an eccentricity ratio of $\epsilon = 0.8$ and are compared with the reported results of Vijayaraghavan and Keith [18] for a 150×8 grid.

Case 2-2: Axially grooved journal bearing with pressured groove (with reformation)

If the supplied oil pressure at the groove is greater than the atmospheric pressure, a reformation boundary appears at a location other than the groove. In this case, locating the reformation boundary is difficult since the reformation front changes position with solution evolution and hence makes it a more challenging problem to be numerically solved and to reach the desired convergence. Similar performance analysis was carried out for a journal bearing with pressurized grooves at $\bar{P}_g = 2\pi$ and the results are tabulated in Table 4 against results of Vijayaraghavan and Keith [18].

The pressure distribution on journal surface for both the nonpressured groove and pressured grooved journal bearings are shown in Fig. 10 for a Mesh size of 50×20.

Direct comparison of the predicted parameters for both nonpressured and pressured supply groove journal bearings as in Tables 3 and 4 can reveal the significant importance of the chosen values for the lubricant bulk modulus on reported results. Such dependency has been denied [18], has not paid adequate attention to and therefore ignored [14,28], or fully acknowledged [19,20,22] in the literature. To better illustrate this, two solution parameters that are most sensitive to the chosen value of the bulk modulus are chosen ($P_{\max}$ and S) and the error in obtaining them for a range of applied lubricant bulk modulus is calculated and is shown in Fig. 11. The reference value for error estimation was

Table 2 Sliding bearing physical and geometrical parameters as in Ref. [25]

Case	$h_{\max}$(mm)	$h_{\min}$(mm)	a(mm)	μ (Pa· s)	U(m/s)	P_c(MPa)	$P_0 = P_a$(MPa)
1-1	0.025	0.015	125	0.015	4	0	0
1-2	0.025	0.015	125	0.015	4	0	1

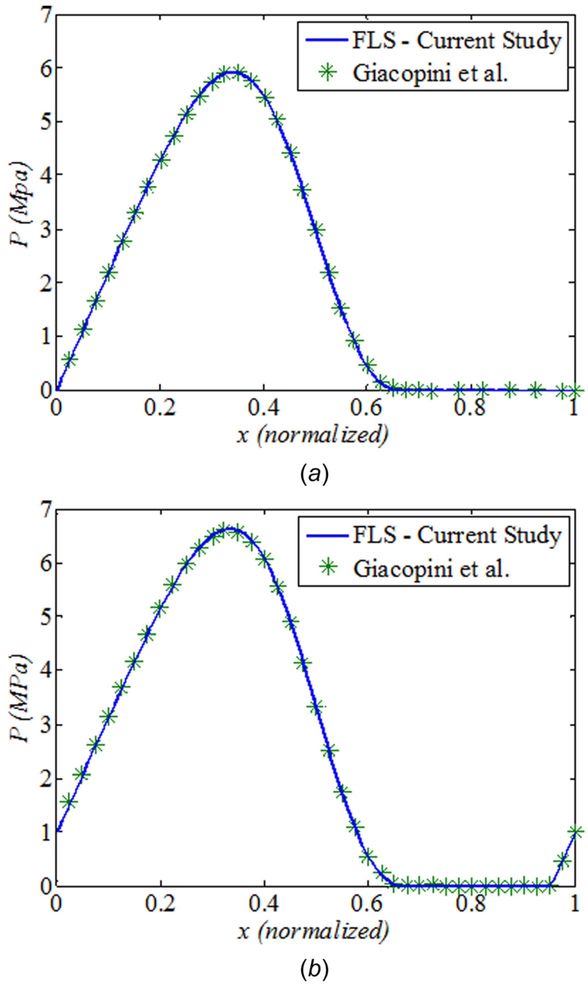

Fig. 9 Comparison of the calculated film pressure based on the FLS in the current study versus the LCP based results of Giacopini et al. [25] for case 1-1, (*a*) and 1-2, (*b*)

chosen to be the converged values at physical lubricant bulk modulus of $\beta = 2$ GPa such that

$$\text{Error} = \frac{u|_{\beta^*} - u|_{\beta_{\text{physical}}}}{u|_{\beta_{\text{physical}}}} \tag{33}$$

where β^* is the bulk modulus value used for analysis. The converged values of pressure distribution at journal midspan against lubricant bulk modulus are shown in Fig. 11.

The variation of calculated error in solution parameters versus the bulk modulus as in Fig. 11(*a*) suggests that the β dependency is significant for very low values of β and by increasing the lubricant bulk modulus toward $\beta = 2 \times 10^7$ and beyond, the error in obtaining the solution drops below 3% in magnitude. As increasing β is crucial in obtaining the correct solution, the inherit numerical difficulty associated with higher β values becomes problematic for the AF based scheme while it almost has no effect on the proposed FLS based scheme and hence a great indicator for robustness of the proposed numerical scheme. Although β dependency for cavitation solution from Elrod algorithm has been previously addressed [19,20,22], a thorough quantitative stability analysis is missing in the literature. Implementing the FLS scheme has a second advantage over the AF schemes since the full coefficient matrices that are constructed during the solution procedure represent the numerical scheme as a whole and are ideal for eigenvalue analysis [33], which is required to assess the stability of a numerical scheme. This is further addressed in Sec. 4.4.

Case 3: High eccentric journal bearing with pressurized groove

The ultimate test for the efficacy and robustness of the FLS based algorithm is to solve for the combination of stiff numerical system with physical bulk modulus of $\beta = 2$ GPa under high eccentricity ratios of $\epsilon = 0.9 \sim 0.99$ with a pressurized groove of $\bar{P}_g = 20\ \pi$ where the cavitation reformation boundary is to be captured. Calculated pressure contours and corresponding convergence plots for a range of eccentricity ratios are given in Fig. 12. Results of Fig. 12 are all obtained for a finer mesh of 100×40. This particular choice of mesh was indeed required to accurately

Table 3 Comparison of predicted parameters of a nonpressurized grooved journal bearing

	Current study		Current study		Current study	Ref. [18]
β	20 MPa		30 MPa		2 GPa	$\equiv$ 30 MPa
Solution method	AF	FLS	AF	FLS	FLS	AF
$\bar{P}_{\max}$	72.2759	72.4370	71.4976	71.4976	69.6741	70.18
S	0.0364	0.0362	0.0366	0.0366	0.0374	—
$\bar{W}$	7.5823	7.6081	7.5265	7.5265	7.3645	7.14
Cav. location ($\bar{x}$)	0.5433	0.5500	0.5500	0.5500	0.5500	0.553
Ref. location ($\bar{x}$)	—	—	—	—	—	—
Time steps to steady-state	2108	93	3104	94	144	2354

Table 4 Comparison of predicted parameters of a pressurized grooved journal bearing

	Current study		Current study		Current study	Ref. [18]
β	20 MPa		30 MPa		2 GPa	$\equiv$ 30 MPa
Solution method	AF	FLS	AF	FLS	FLS	AF
$\bar{P}_{\max}$	73.0067	73.1731	72.2094	72.2094	70.3793	70.81
S	0.0324	0.0323	0.0326	0.0326	0.0333	—
$\bar{W}$	7.3145	7.3394	7.2597	7.2598	7.1018	6.87
Cav. location ($\bar{x}$)	0.5433	0.5500	0.5500	0.5500	0.5500	0.553
Ref. location ($\bar{x}$)	0.9100	0.9100	0.9100	0.9100	0.9100	0.900
Time steps to steady-state	4950	235	7429	264	428	10,380

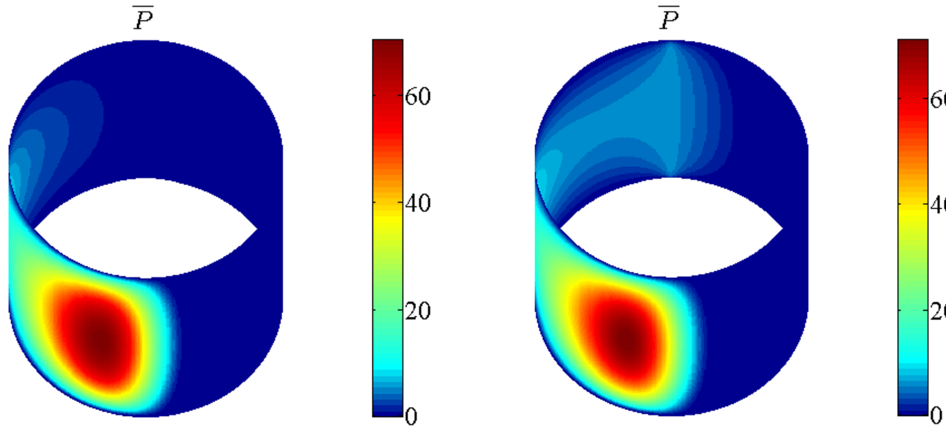

(*a*) (*b*)

Fig. 10 Pressure distribution of a nonpressured supply groove journal bearing of case 2-1 (*a*) and for a pressurized supply groove with *Pg* = 2 π of case 2-2 (*b*) both at $\epsilon = 0.8$ with a physical choice of bulk modulus $\beta = 2$ GPa

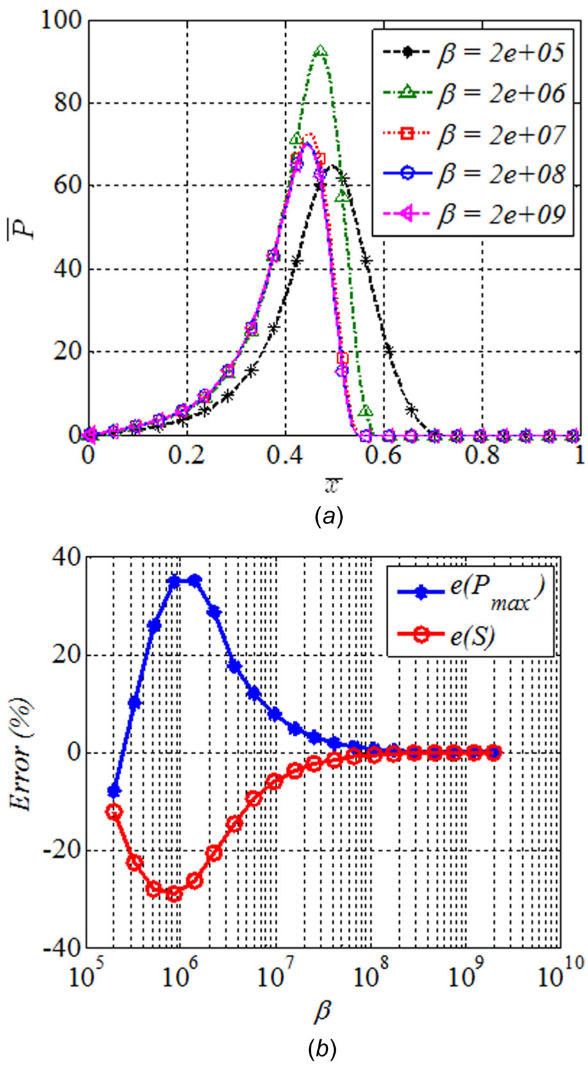

Fig. 11 Error in obtaining solution parameters versus choice of bulk modulus, β (*a*) and pressure variation at midspan with β (*b*)

capture the high pressure gradients in high eccentric devices. Based on the convergence plots of Fig. 12(*b*), it can be easily inferred that the performance of FLS based algorithm is not affected by the choice of eccentricity ratio. However, the difficulty in resolving the reformation boundary demands more iterations to reach convergence compared to the unpressurized cases of Fig. 5.

4.4 Numerical Stability of the Cavitation Algorithm. A numerical stability analysis is performed based on the eigenvalue analysis of the coefficient matrix for a pressurized grooved journal bearing at a range of lubricant bulk modulus values as low as $\beta = 2 \times 10^5$ $(\equiv \bar{\beta} = 2.75)$ up to $\beta = 2 \times 10^9$ $(\equiv \bar{\beta} = 2.75 \times 10^4)$. The coefficient matrix used for analysis needs to be in the form of Eq. (A11) for the eigenvalues to represent the numerical system as a whole. The calculated eigenvalues are depicted in Fig. 13.

By analysing the eigenvalues λ of Fig. 13, it is evident that there is a space structure to the calculated eigenvalues, being spread on both real and imaginary axis as in Figs. 13(*a*)–13(*c*) and yet maintaining a structure close to the origin as shown in Fig. 13(*d*). It can be also seen that as the bulk modulus increases in magnitude, the space span of the eigenvalues expands in both real and imaginary axis and shifts leftward toward the origin on the real axis. An increase in the real part of the eigenvalues as well as an increase in their imaginary part at the same time is associated to the coexistence of lower and higher frequency harmonics with

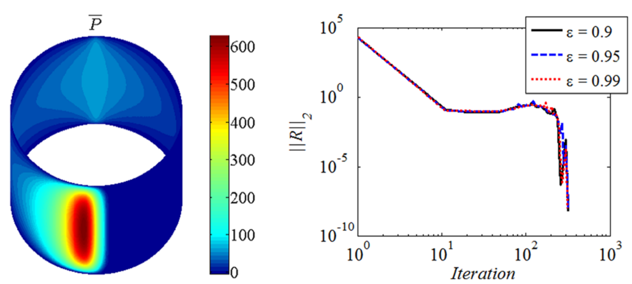

(*a*) (*b*)

Fig. 12 Pressure contours for a high eccentric journal bearing at $\epsilon = 0.95$ with pressurized groove at *Pg* = 20 π and physical bulk modulus of $\beta = 2$ GPa (*a*) and the corresponding convergence plots for a range of eccentricity ratios (*b*)

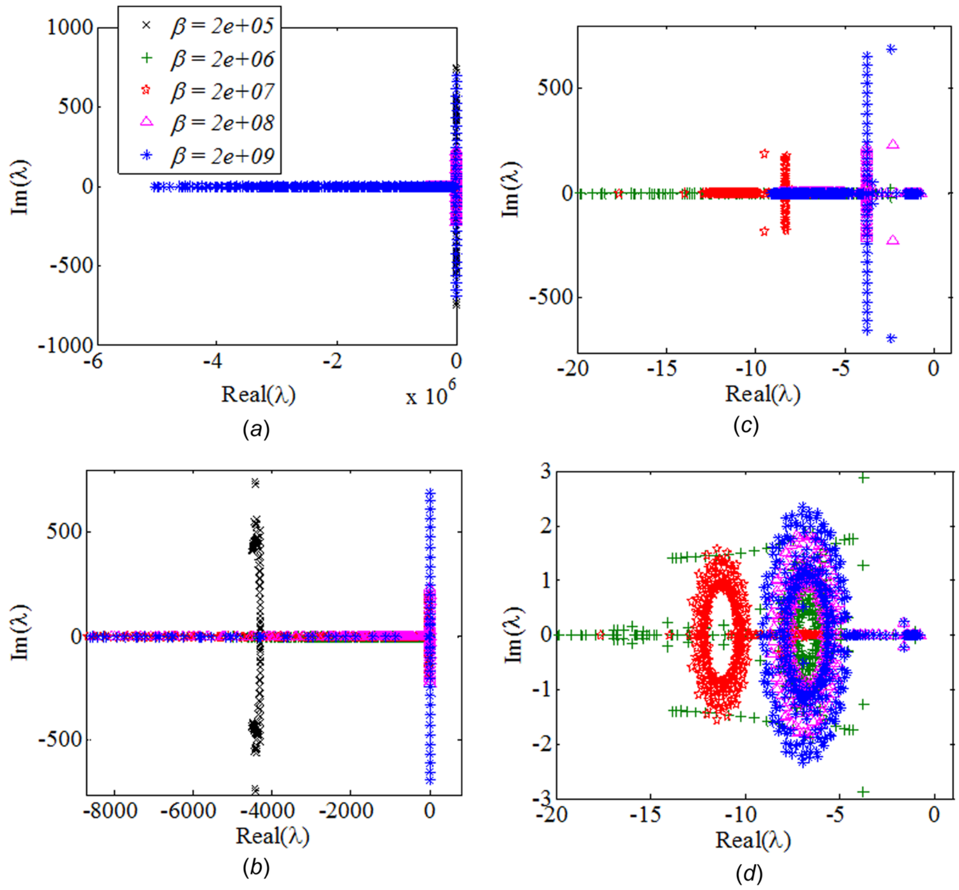

Fig. 13 Eigenvalues of the full linear system for a range of lubricant bulk modulus

higher amplitudes in the solution i.e. increased difficulty to resolve the errors. As a result, schemes that are inherently problematic in dealing with low frequency errors like Approximate Factorization are not suitable for the cavitation problem. Another indicator for numerical difficulty in obtaining the solution is high values of numerical stiffness.

Defining stiffness of a numerical scheme as $K_{\text{num}} = \max(|\text{Re}(\lambda)|)\ /\min(|\text{Re}(\lambda)|)$, it can be shown how stiffness increases exponentially with increasing bulk modulus as shown in Fig. 14(*a*) for a range of eccentricity ratios. The effect of the applied load i.e. eccentricity ratio on numerical stiffness for a range of selected bulk moduli is shown in Fig. 14(*b*) as well as the choice of number of elements in both x and z directions in Figs. 14(*c*) and 14(*d*). A 100×40 mesh was used to calculate the results of Figs. 14(*a*) and 14(*b*) and a bulk modulus of $\beta = 2$ GPa was used for the calculations in Figs. 14(*c*) and 14(*d*). Since Figs. 14(*c*) and 14(*d*) are designed to study the change of numerical stiffness versus M_x and M_z, the mesh divisions in the alternate direction is to be kept constant and was set to $M_z = 40$ and $M_x = 100$ for Figs. 14(*c*) and 14(*d*), respectively.

From the numerical stiffness results of Fig. 14, it can be identified that increasing static load renders the numerical system slightly stiffer but not with a great margin. It can also be seen from Figs. 14(*c*) and 14(*d*) that the choice of mesh size in both directions is insignificant in numerical stiffness. However as expected, an order of magnitude increase in lubricant bulk modulus significantly increases the stiffness of the numerical system regardless of the static load (i.e. eccentricity ratio). In order to maintain the stability of such stiff numerical system, solvers are usually forced to choose unreasonably small time steps which leads to very slow convergence. In the lubrication problem where accuracy of results depend on the physical choice of the bulk modulus, the inevitable stiff discretized numerical system needs to be solved efficiently by means of well adopted schemes as the one proposed in this paper.

5 Conclusion

In the current study, a modified fast converging and robust algorithm was proposed for solving the cavitation problem in axially grooved journal bearings based on the finite volume method (FVM). Detailed discretization of the Adams/Elrod cavitation algorithm with Vijayaraghavan and Keith treatment was derived and presented based on the FVM. The solution of cavitation problem was shown to strongly depend on the specific values chosen for the bulk modulus of the lubricant. Since the realistic and physical values of the bulk modulus can render the discretized system of equations too stiff and therefore numerically very difficult to solve, many researchers used artificially low values of β to cope with this difficulty. This was demonstrated by studying the stiff and artificially softened system and solving them by both AF based scheme and the proposed scheme. It was shown how the new proposed scheme that is based on the direct solve of the full linear system is capable of handling the stiff system for any chosen value of the bulk modulus β. The new scheme showed a significant improvement in the robustness compared to traditionally used Approximate Factorization based schemes. Calculations were carried out for journal bearings with pressurized supply oil and with atmospheric supplied lubricant. In the pressurized case, the reformation boundary was particularly difficult to resolve with the AF based scheme whereas the FLS scheme showed almost no change in its convergence behavior.

The numerical stability of the fully discretized system was also analyzed by means of eigenvalue analysis of the coefficient matrix of the full linear system. It was shown that by increasing the bulk modulus, the space span of the eigenvalues of the system both

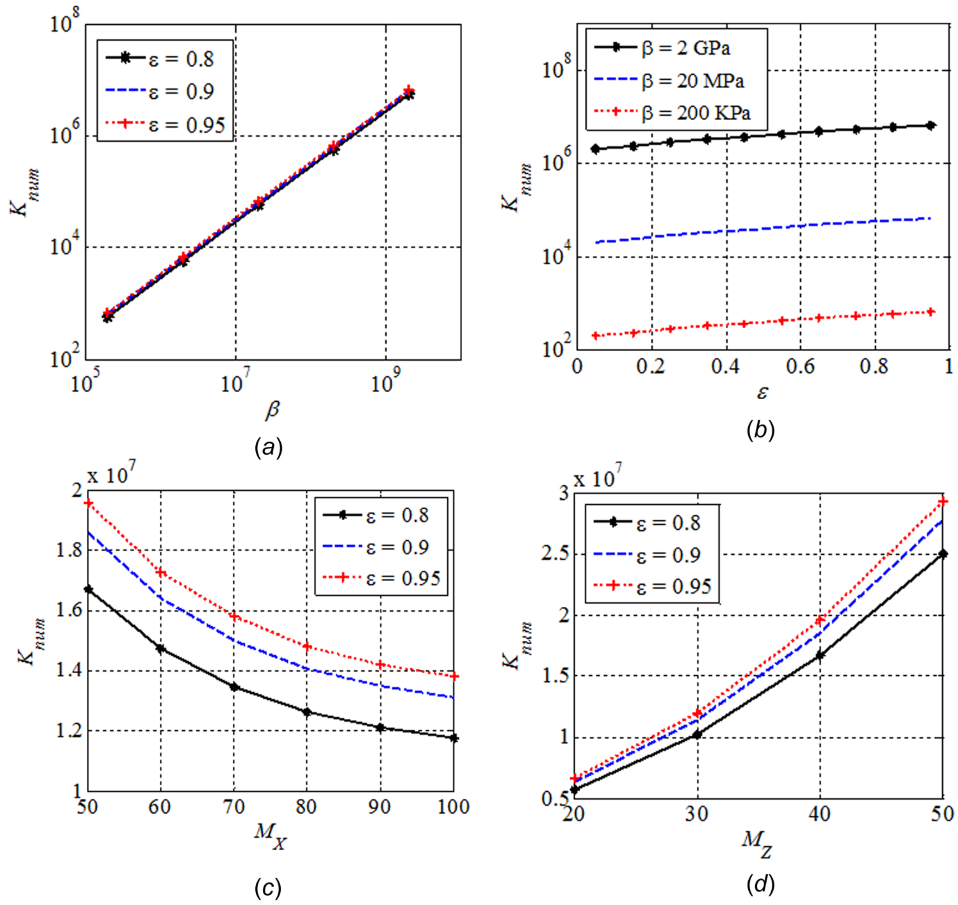

Fig. 14 Numerical stiffness versus the lubricant bulk modulus (*a*), eccentricity ratios (*b*), and number of mesh elements in *x* (*c*) and *z* directions *x* (*d*)

expands and shifts toward the right half plane as a clear indicator for difficulty in the convergence of the discretized numerical system. Effects of static load and mesh size were also studied on the stability of the system and it was found that their impact is negligible compared to dominant significance of varying bulk modulus values. By studying the numerical error caused by the artificial choice of lower bulk modulus values, it was found that a reduction of maximum two order of magnitudes can be tolerated to prevent the final solution from deviating more than 3% from the ideal case with physically chosen values for lubricant bulk modulus.

Acknowledgment

The authors would like to thank Qatar National Research Fund (QNRF) for partially funding this project. Also, many thanks to Mohammad Fesanghari from Louisiana State University for fruitful discussions on different aspects of available discretizations of the Adams/Elrod cavitation algorithm.

Nomenclature

C = radial clearance (m)
D = journal bearing diameter (m)
D_x, D_z = decoupled coefficient matrices of the discretized PDE system in x and z directions
e = eccentricity (m)
$\%e_{\text{ext}}{}^{21}, e_{\text{ext}}{}^{21}$ = coarse and fine grid extrapolated relative errors in numerical calculation of the field variable
$F, F_{i\pm\frac{1}{2},j}$ = x-component of the flux vector and its value at control volume interfaces
$\mathbf{FI}, FI^n$ = flux integral vector and control volume average flux integral at time-step n
$G, G_{i,j\pm\frac{1}{2}}$ = z-component of the flux vector and its value at control volume interfaces
$\text{GCI}_{\text{coarse}}{}^{32}, \text{GCI}_{\text{fine}}{}^{21}$ = coarse and fine grid convergence index
g = gFactor
h = oil film thickness, $h = C(1 + \epsilon\cos(\theta))$ (m)
H = nondimensional oil thickness $H = h/C$
K_{num} = numerical stiffness
L = journal bearing length (m)
m, n = number of elements in x and z directions
N = rotating speed (rev/s)
$P, \bar{P}$ = bearing induced pressure and its nondimensional form $\bar{\text{P}} = \text{P}/\ \mu\ N\ (R/C)^2$
$\bar{P}_{\max}, \bar{P}_g$ = nondimensional maximum pressure and supply groove pressure
R = journal radius (m)
$R(U), \|R(U)\|_2$ = residual matrix and the L_2 norm of the residual
S = Sommerfeld number $S = L\ D\ \mu\ N/W(R/C)^2$
$t, \bar{t}$ = time (s) and its nondimensional form: $\bar{t} = \omega\ t$
$u, \bar{u}$ = solution to the governing PDE and its control volume average
$\tilde{u}, \tilde{U}$ = axillary control volume solution and its vector representation

$\mathbf{U}$, $\delta\mathbf{U}$ = control volumes solution vector and the change in solution vector
$W, \bar{W}$ = bearing load capacity (N) and its nondimensional form: $\bar{W} = W/L\ D\ \mu\ \omega(C/R)^2$
x, z = circumferential and axial directions in space
$\bar{x}$, $\bar{z}$ = dimensionless circumferential and axial directions in space
X_i = coefficients of the linear discretized system in x direction. $i = -2, -1, 0, 1$
Z_j = coefficients of the linear discretized system in z direction. $j = -1, 0, 1$
α = fluid density ratio: $\alpha = \rho/\rho_c$
β, $\bar{\beta}$ = lubricant bulk modulus (Pa) and its nondimensional form: $\bar{\beta} = \beta/\mu\omega(C/R)^2$
ϵ = eccentricity ratio $\epsilon = e/C$
θ, θ_{cav} = circumferential coordinate and the cavitation boundary
λ = eigenvalues of the discretized system coefficient matrix
μ = fluid film (lubricant) viscosity (Pa·s)
ρ, ρ_c = fluid film density (kg/m^3) and film viscosity at cavitation pressure
$\Phi_{ext}{}^{21}$ = extrapolated field variable in fine grid
Φ_1, Φ_2, Φ_3 = numerical estimate of the field variable in fine, medium and coarse mesh
ω = shaft rotating speed (rad/s)
ω_r = under-relaxation parameter

Appendix

To simplify notation it is useful to define

$$H_{i+1/2,j} = \frac{H_{i+1,j} + H_{i,j}}{2};\ \text{and}\ \ H_{i,j+1/2} = \frac{H_{i,j+1} + H_{i,j}}{2}$$
$$H_{i-1/2,j} = \frac{H_{i-1,j} + H_{i,j}}{2};\ \text{and}\ \ H_{i,j-1/2} = \frac{H_{i,j-1} + H_{i,j}}{2} \quad (A1)$$
$$g_{i+1/2,j} = \frac{g_{i+1,j} + g_{i,j}}{2};\ \text{and}\ \ g_{i-1/2,j} = \frac{g_{i-1,j} + g_{i,j}}{2}$$

Recall from Eq. (23)

$$u = \alpha H$$
$$F = \frac{u}{4\pi} - \frac{\beta}{48\pi^2}\ H^3\frac{\partial g(\alpha-1)}{\partial x} - (1-g)\left(\frac{\partial^2 u}{\partial x^2}\ \frac{\Delta x^2}{3} - \frac{\partial^3 u}{\partial x^3}\ \frac{\Delta x^3}{4}\right)$$
$$G = \frac{\beta}{48\ (L/D)^2}H^3\frac{\partial g(\alpha-1)}{\partial z} \quad (A2)$$

Hence, the fluxes at control surface boundaries using a central differencing formulation can be written as

$$F_{i+\frac{1}{2},j} = \frac{1}{4\pi}\left(\frac{\alpha_{i,j}H_{i,j} + \alpha_{i+1,j}H_{i+1,j}}{2}\right) - \frac{\beta H_{i+\frac{1}{2},j}{}^3}{48\pi^2}\left(\frac{(\alpha_{i+1,j}-1)g_{i+1,j} - (\alpha_{i,j}-1)g_{i,j}}{\Delta x}\right) - \frac{1-g_{i+1/2,j}}{4\pi}\left(\frac{\alpha_{i-1,j}H_{i-1,j} - 2\alpha_{i,j}H_{i,j} + \alpha_{i+1,j}H_{i+1,j}}{2}\right)$$
$$F_{i-\frac{1}{2},j} = \frac{1}{4\pi}\left(\frac{\alpha_{i-1,j}H_{i-1,j} + \alpha_{i,j}H_{i,j}}{2}\right) - \frac{\beta H_{i-\frac{1}{2},j}{}^3}{48\pi^2}\left(\frac{(\alpha_{i,j}-1)g_{i,j} - (\alpha_{i-1,j}-1)g_{i-1,j}}{\Delta x}\right) - \frac{1-g_{i-1/2,j}}{4\pi}\left(\frac{\alpha_{i-2,j}H_{i-2,j} - 2\alpha_{i-1,j}H_{i-1,j} + \alpha_{i,j}H_{i,j}}{2}\right)$$
$$G_{i,j+\frac{1}{2}} = \frac{-\beta H_{i,j+\frac{1}{2}}{}^3}{48\ (L/D)^2}\left(\frac{(\alpha_{i,j+1}-1)g_{i,j+1} - (\alpha_{i,j}-1)g_{i,j}}{\Delta z}\right)$$
$$G_{i,j-\frac{1}{2}} = \frac{-\beta H_{i,j-\frac{1}{2}}{}^3}{48\ (L/D)^2}\left(\frac{(\alpha_{i,j}-1)g_{i,j} - (\alpha_{i,j-1}-1)g_{i,j-1}}{\Delta z}\right) \quad (A3)$$

The higher-order artificial viscosity terms in $F_{i+\frac{1}{2},j}$ and $F_{i-\frac{1}{2},j}$ of Eq. (A3) are chosen such that by substituting $g = 0$ in the shear term at cavitation zone, the second-order accurate centrally differenced derivative be reduced to a second-order upwind difference

$$\frac{\partial u}{\partial x} = \left.\frac{F_{i+\frac{1}{2},j} - F_{i-\frac{1}{2},j}}{\Delta x}\right|_{g=0} = \frac{1}{4\pi}\frac{\alpha_{i-2,j}H_{i-2,j} - 4\alpha_{i-1,j}H_{i-1,j} + 3\alpha_{i,j}H_{i,j}}{2\ \ \Delta x} \quad (A4)$$

Hence, it satisfies the upwind differencing in the hyperbolic cavitation zone as proposed by Vijayaraghavan and Keith [15,26]. The values of the fluxes at the control surface boundaries in Eq. (A3) is then to be substituted in the space-time discretized system of Eq. (21); dropping all the superscripts knowing that all the terms are evaluated at the current time-step we can write

$$\delta\bar{u}_{i,j}\left(\frac{1}{\Delta t} + \frac{1}{\Delta x}\frac{\partial F_{i+\frac{1}{2},j}}{\partial \bar{u}_{i,j}} - \frac{1}{\Delta x}\frac{\partial F_{i-\frac{1}{2},j}}{\partial \bar{u}_{i,j}} + \frac{1}{\Delta z}\frac{\partial G_{i,j+\frac{1}{2}}}{\partial \bar{u}_{i,j}} - \frac{1}{\Delta z}\frac{\partial G_{i,j-\frac{1}{2}}}{\partial \bar{u}_{i,j}}\right) + \frac{1}{\Delta x}\frac{\partial F_{i+\frac{1}{2},j}}{\partial \bar{u}_{i+1,j}}\delta\bar{u}_{i+1,j} - \frac{1}{\Delta x}\frac{\partial F_{i-\frac{1}{2},j}}{\partial \bar{u}_{i-1,j}}\delta\bar{u}_{i-1,j} + \frac{1}{\Delta z}\frac{\partial G_{i,j+\frac{1}{2}}}{\partial \bar{u}_{i,j+1}}\delta\bar{u}_{i,j+1}$$
$$-\frac{1}{\Delta z}\frac{\partial G_{i,j-\frac{1}{2}}}{\partial \bar{u}_{i,j-1}}\delta\bar{u}_{i,j-1} = -\frac{F_{i+\frac{1}{2},j} - F_{i-\frac{1}{2},j}}{\Delta x} - \frac{G_{i,j+\frac{1}{2}} - G_{i,j-\frac{1}{2}}}{\Delta z} \quad (A5)$$

where the right-hand side (RHS) of Eq. (A5) is the flux integral and can be written in its final form as

$$
\begin{aligned}
\mathrm{RHS} = FI = & -\frac{\beta g_{-1+i,j} H^3_{i-\frac{1}{2},j}}{48\pi^2 \Delta x^2} + \frac{\beta g_{i,j} H^3_{i-\frac{1}{2},j}}{48\pi^2 \Delta x^2} - \frac{\beta g_{i,-1+j} H^3_{i,j-\frac{1}{2}}}{48\left(\frac{L}{D}\right)^2 \Delta z^2} + \frac{\beta g_{i,j} H^3_{i,j-\frac{1}{2}}}{48\left(\frac{L}{D}\right)^2 \Delta z^2} \\
& + \frac{\beta g_{i,j} H^3_{i,j+\frac{1}{2}}}{48\left(\frac{L}{D}\right)^2 \Delta z^2} - \frac{\beta g_{i,1+j} H^3_{i,j+\frac{1}{2}}}{48\left(\frac{L}{D}\right)^2 \Delta z^2} + \frac{\beta g_{i,j} H^3_{i+\frac{1}{2},j}}{48\pi^2 \Delta x^2} - \frac{\beta g_{1+i,j} H^3_{i+\frac{1}{2},j}}{48\pi^2 \Delta x^2} + \left(-\frac{H_{i-2,j}}{8\pi\Delta x} + \frac{g_{i-\frac{1}{2},j} H_{i-2,j}}{8\pi\Delta x}\right)\alpha_{i-2,j} \\
& + \left(\frac{H_{i-1,j}}{2\pi\Delta x} - \frac{g_{i-\frac{1}{2},j} H_{i-1,j}}{4\pi\Delta x} - \frac{g_{i+\frac{1}{2},j} H_{i-1,j}}{8\pi\Delta x} + \frac{\beta g_{i-1,j} H^3_{i-\frac{1}{2},j}}{48\pi^2 \Delta x^2}\right)\alpha_{i-1,j} \\
& + \left(-\frac{\beta g_{i,j} H^3_{i-\frac{1}{2},j}}{48\pi^2 \Delta x^2} - \frac{\beta g_{i,j} H^3_{i,j-\frac{1}{2}}}{48\left(\frac{L}{D}\right)^2 \Delta z^2} - \frac{3H_{i,j}}{8\pi\Delta x} + \frac{g_{i-\frac{1}{2},j} H_{i,j}}{8\pi\Delta x} + \frac{g_{i+\frac{1}{2},j} H_{i,j}}{4\pi\Delta x} - \frac{\beta g_{i,j} H^3_{i,j+\frac{1}{2}}}{48\left(\frac{L}{D}\right)^2 \Delta z^2} - \frac{\beta g_{i,j} H^3_{i+\frac{1}{2},j}}{48\pi^2 \Delta x^2}\right)\alpha_{i,j} + \left(\frac{\beta g_{i+1,j} H^3_{i+\frac{1}{2},j}}{48\pi^2 \Delta x^2} - \frac{g_{i+\frac{1}{2},j} H_{1+i,j}}{8\pi\Delta x}\right)\alpha_{i+1,j} \\
& + \frac{\beta g_{i,j-1} H^3_{i,-\frac{1}{2}+j}}{48\left(\frac{L}{D}\right)^2 \Delta z^2}\alpha_{i,j-1} + \frac{\beta g_{i,j+1} H^3_{i,j+\frac{1}{2}}}{48\left(\frac{L}{D}\right)^2 \Delta z^2}\alpha_{i,j+1}
\end{aligned}
\tag{A6}
$$

Carrying out the partial derivations in the LHS of Eq. (A5) we will have

$$
\frac{\partial F_{i+\frac{1}{2},j}}{\partial \bar{u}_{i,j}} = \frac{\partial F_{i+\frac{1}{2},j}}{\partial \alpha_{i,j} H_{i,j}} = \frac{6\pi\Delta x\left(3 - 2g_{i+\frac{1}{2},j}\right)H_{i,j} + \beta g_{i,j} H^3_{i+\frac{1}{2},j}}{48\pi^2 \Delta x \; H_{i,j}}
\tag{A7}
$$

and similarly for all the other partial derivative terms. Hence, the LHS in its final form can be written as

$$
\mathrm{LHS} = X_{-2}\;\delta u_{i-2,j} + X_{-1}\;\delta u_{i-1,j} + XZ_0\;\delta u_{i,j} + X_{+1}\;\delta u_{i+1,j} + Y_{-1}\;\delta u_{i,j-1} + Y_{-2}\;\delta u_{i,j+1}
\tag{A8}
$$

where

$$
\begin{aligned}
& X_{-2} = -\frac{\left(-1 + g_{i-\frac{1}{2},j}\right)}{8\pi\;\Delta x} \quad X_{-1} = \left(\frac{-1 + g_{i+\frac{1}{2},j}}{8\pi\;\Delta x} - \frac{6\pi\Delta x\;\left(3 - 2g_{i-\frac{1}{2},j}\right)\;H_{-1+i,j} + \beta g_{-1+i,j}\;H^3_{i-\frac{1}{2},j}}{48\;\pi^2 \Delta x^2\;H_{i-1,j}}\right) \\
& XZ_0 = \left(\frac{1}{\Delta t} + \frac{\beta g_{i,j}\;H^3_{i,j-\frac{1}{2}}}{48\left(\frac{L}{D}\right)^2 \Delta z^2 H_{i,j}} - \frac{-\beta g_{i,j} H^3_{i-\frac{1}{2},j} + 6\pi\;\Delta x\;g_{i-\frac{1}{2},j} H_{i,j}}{48\pi^2 \Delta x^2 H_{i,j}} + \frac{\beta g_{i,j}\;H^3_{i,j+\frac{1}{2}}}{48\;\left(\frac{L}{D}\right)^2\;\Delta z^2 H_{i,j}} + \frac{6\pi\;\Delta x\;\left(3 - 2g_{i+\frac{1}{2},j}\right)\;H_{i,j} + \beta g_{i,j} H^3_{i+\frac{1}{2},j}}{48\pi^2 \Delta x^2 H_{i,j}}\right) \\
& X_{+1} = \frac{\left(-\beta g_{i+1,j}\;H^3_{i+\frac{1}{2},j} + 6\pi\;\Delta x\;g_{i+\frac{1}{2},j} H_{1+i,j}\right)}{48\;\pi^2 \Delta x^2\;H_{i+1,j}} \quad Z_{-1} = -\frac{\beta g_{i,j-1}\;H^3_{i,j-\frac{1}{2}}}{48\;\left(\frac{L}{D}\right)^2\;\Delta z^2 H_{i,j-1}} \quad Z_{+1} = -\frac{\beta g_{i,j+1}\;H^3_{i,j+\frac{1}{2}}}{48\;(L/D)^2\;\Delta z^2\;H_{i,j+1}}
\end{aligned}
\tag{A9}
$$

Hence, the final fully discretized Reynolds equation can be written as

$$
\begin{aligned}
& X_{-2}\;\delta\Phi_{i-2,j} + X_{-1}\;\delta\Phi_{i-1,j} + XZ_0\;\delta\Phi_{i,j} + X_{+1}\;\delta\Phi_{i+1,j} \\
& \quad + Z_{-1}\;\delta\Phi_{i,j-1} + Z_{-2}\;\delta\Phi_{i,j+1} = FI
\end{aligned}
\tag{A10}
$$

Now, as an example, considering a 2D mesh of size 4×4 as a subset of a bigger mesh as shown in Fig. 15.

One can form the full linear system for a 4×4 mesh as

$$
[A][\delta u] = [FI]
\tag{A11}
$$

where

(1,1)	(1,2)	(1,3)	(1,4)
(2,1)	(2,2)	(2,3)	(2,4)
(3,1)	(3,2)	(3,3)	(3,4)
(4,1)	(4,2)	(4,3)	(4,4)

Fig. 15 A 4×4 mesh

$$[A]=\left[\begin{array}{cccccccccccccccc}
XZ_0 & X_{+1} & & & Z_1 & & & & & & & & & & & \\
X_{-1} & XZ_0 & X_{+1} & & & Z_1 & & & & & & & & & & \\
X_{-2} & X_{-1} & XZ_0 & X_{+1} & & & Z_1 & & & & & & & & & \\
 & X_{-2} & X_{-1} & XZ_0 & & & & Z_1 & & & & & & & & \\
Z_{-1} & & & & XZ_0 & X_{+1} & & & Z_1 & & & & & & & \\
 & Z_{-1} & & & X_{-1} & XZ_0 & X_{+1} & & & Z_1 & & & & & & \\
 & & Z_{-1} & & X_{-2} & X_{-1} & XZ_0 & X_{+1} & & & Z_1 & & & & & \\
 & & & Z_{-1} & & X_{-2} & X_{-1} & XZ_0 & & & & Z_1 & & & & \\
 & & & & Z_{-1} & & & & XZ_0 & X_{+1} & & & Z_1 & & & \\
 & & & & & Z_{-1} & & & X_{-1} & XZ_0 & X_{+1} & & & Z_1 & & \\
 & & & & & & Z_{-1} & & X_{-2} & X_{-1} & XZ_0 & X_{+1} & & & Z_1 & \\
 & & & & & & & Z_{-1} & & X_{-2} & X_{-1} & XZ_0 & & & & Z_1 \\
 & & & & & & & & Z_{-1} & & & & XZ_0 & X_{+1} & & \\
 & & & & & & & & & Z_{-1} & & & X_{-1} & XZ_0 & X_{+1} & \\
 & & & & & & & & & & Z_{-1} & & X_{-2} & X_{-1} & XZ_0 & X_{+1} \\
 & & & & & & & & & & & Z_{-1} & & X_{-2} & X_{-1} & XZ_0
\end{array}\right] \tag{A12}$$

and

$$[\delta u]=\begin{bmatrix}\delta u_{1,1}\\ \delta u_{2,1}\\ \delta u_{3,1}\\ \delta u_{4,1}\\ \delta u_{1,2}\\ \delta u_{2,2}\\ \delta u_{3,2}\\ \delta u_{4,2}\\ \delta u_{1,3}\\ \delta u_{2,3}\\ \delta u_{3,3}\\ \delta u_{4,3}\\ \delta u_{1,4}\\ \delta u_{2,4}\\ \delta u_{3,4}\\ \delta u_{4,4}\end{bmatrix};[FI]=\begin{bmatrix}FI_{1,1}\\ FI_{2,1}\\ FI_{3,1}\\ FI_{4,1}\\ FI_{1,2}\\ FI_{2,2}\\ FI_{3,2}\\ FI_{4,2}\\ FI_{1,3}\\ FI_{2,3}\\ FI_{3,3}\\ FI_{4,3}\\ FI_{1,4}\\ FI_{2,4}\\ FI_{3,4}\\ FI_{4,4}\end{bmatrix} \tag{A13}$$

References

[1] Temperley, H., and Trevena, D., 1977, "Metastability of Phase Transitions and the Tensile Strength of Liquids," Proc. R. Soc. London, Ser. A, **357**(1690), pp. 395–402.

[2] Braun, M., and Hannon, W., 2010, "Cavitation Formation and Modelling for Fluid Film Bearings: A Review," Proc. Inst. Mech. Eng., Part J, **224**(9), pp. 839–863.

[3] Brewe, D. E., 1986, "Theoretical Modeling of the Vapor Cavitation in Dynamically Loaded Journal Bearings," ASME J. Tribol., **108**(4), pp. 628–637.

[4] Szeri, A. Z., 2011, *Fluid Film Lubrication*, Cambridge University Press, Cambridge, UK.

[5] Christopherson, D. G., 1941, "A New Mathematical Method for the Solution of Film Lubrication Problems," Proc. Inst. Mech. Eng., **146**(1), pp. 126–135.

[6] Ausas, R., Ragot, P., Leiva, J., Jai, M., Bayada, G., and Buscaglia, G. C., 2007, "The Impact of the Cavitation Model in the Analysis of Microtextured Lubricated Journal Bearings," ASME J. Tribol., **129**(4), pp. 868–875.

[7] Ausas, R. F., Jai, M., and Buscaglia, G. C., 2009, "A Mass-Conserving Algorithm for Dynamical Lubrication Problems With Cavitation," ASME J. Tribol., **131**(3), p. 031702.

[8] Jakobsson, B., and Floberg, L., 1957, The Finite Journal Bearing Considering Vaporization (Transactions of Chalmers University of Technology), Vol. 190, Guthenberg, Sweden, p. 308.

[9] Olsson, K. O., 1965, Cavitation in Dynamically Loaded Bearing (Transactions of Chalmers University of Technology), Vol. 308, Guthenberg, Sweden, p. 308.

[10] Etsion, I., and Ludwig, L., 1982, "Observation of Pressure Variation in the Cavitation Region of Submerged Journal Bearings," ASME J. Lubr. Technol., **104**(2), pp. 157–163.

[11] Elrod, H., and Adams, M., 1974, "A Computer Program for Cavitation and Starvation Problems," *Cavitation and Related Phenomena in Lubrication*, Mechanical Engineering Publications, New York, pp. 37–41.

[12] Elrod, H. G., 1981, "A Cavitation Algorithm," ASME J. Tribol., **103**(3), pp. 350–354.

[13] Miranda, A., 1983, "Oil Flow, Cavitation and Film Reformation in Journal Bearings, Including an Interactive Computer-Aided Design Study," Ph.D. thesis, University of Leeds, Leeds, UK.

[14] Hirani, H., Athre, K., and Biswas, S., 2001, "A Simplified Mass Conserving Algorithm for Journal Bearing Under Large Dynamic Loads," Int. J. Rotating Mach., **7**(1), pp. 41–51.

[15] Vijayaraghavan, D., and Keith, T., 1990, "An Efficient, Robust, and Time Accurate Numerical Scheme Applied to a Cavitation Algorithm," ASME J. Tribol., **112**(1), pp. 44–51.

[16] Woods, C. M., and Brewe, D. E., 1989, "The Solution of the Elrod Algorithm for a Dynamically Loaded Journal Bearing Using Multigrid Techniques," ASME J. Tribol., **111**(2), pp. 302–308.

[17] Qiu, Y., and Khonsari, M., 2009, "On the Prediction of Cavitation in Dimples Using a Mass-Conservative Algorithm," ASME J. Tribol., **131**(4), p. 041702.

[18] Vijayaraghavan, D., and Keith, T., 1990, "Grid Transformation and Adaption Techniques Applied in the Analysis of Cavitated Journal Bearings," ASME J. Tribol., **112**(1), pp. 52–59.

[19] Almqvist, A., Fabricius, J., Larsson, R., and Wall, P., 2014, "A New Approach for Studying Cavitation in Lubrication," ASME J. Tribol., **136**(1), p. 011706

[20] Bayada, G., and Chupin, L., 2013, "Compressible Fluid Model for Hydrodynamic Lubrication Cavitation," ASME J. Tribol., **135**(4), p. 041702.

[21] Bertocchi, L., Dini, D., Giacopini, M., Fowell, M. T., and Baldini, A., 2013, "Fluid Film Lubrication in the Presence of Cavitation: A Mass-Conserving Two-Dimensional Formulation for Compressible, Piezoviscous and Non-Newtonian Fluids," Tribol. Int., **67**, pp. 61–71.

[22] Sahlin, F., Almqvist, A., Larsson, R., and Glavatskih, S., 2007, "A Cavitation Algorithm for Arbitrary Lubricant Compressibility," Tribol. Int., **40**(8), pp. 1294–1300.

[23] Bayada, G., 2014, "From a Compressible Fluid Model to New Mass Conserving Cavitation Algorithms," Tribol. Int., **71**, pp. 38–49.

[24] Braun, M., and Hendricks, R., 1984, "An Experimental Investigation of the Vaporous/Gaseous Cavity Characteristics of an Eccentric Journal Bearing," ASLE Trans., **27**(1), pp. 1–14.

[25] Giacopini, M., Fowell, M. T., Dini, D., and Strozzi, A., 2010, "A Mass-Conserving Complementarity Formulation to Study Lubricant Films in the Presence of Cavitation," ASME J. Tribol., **132**(4), p. 041702.

[26] Vijayaraghavan, D., and Keith, T., Jr., 1989, "Development and Evaluation of a Cavitation Algorithm," Tribol. Trans., **32**(2), pp. 225–233.

[27] Ståhl, J., and Jacobson, B. O., 2003, "Compressibility of Lubricants at High Pressures," Tribol. Trans., **46**(4), pp. 592–599.

[28] Rao, T., and Sawicki, J. T., 2002, "Linear Stability Analysis for a Hydrodynamic Journal Bearing Considering Cavitation Effects," Tribol. Trans., **45**(4), pp. 450–456.
[29] Yang, L.-H., Wang, W.-M., Zhao, S.-Q., Sun, Y.-H., and Yu, L., 2014, "A New Nonlinear Dynamic Analysis Method of Rotor System Supported by Oil-Film Journal Bearings," Appl. Math. Modell., **38**(21), pp. 5239–5255.
[30] Ceze, M., and Fidkowski, K. J., 2015, "Constrained Pseudo-Transient Continuation," Int. J. Numer. Methods Eng., **102**(11), pp. 1683–1703.
[31] Fesanghary, M., and Khonsari, M., 2011, "A Modification of the Switch Function in the Elrod Cavitation Algorithm," ASME J. Tribol., **133**(2), p. 024501.
[32] Celik, I. B., Ghia, U., and Roache, P. J., 2008, "Procedure for Estimation and Reporting of Uncertainty Due to Discretization in CFD Applications," ASME J. Fluids Eng., **130**(7), p. 078001.
[33] Jalali, A., Sharbatdar, M., and Ollivier-Gooch, C., 2014, "Accuracy Analysis of Unstructured Finite Volume Discretization Schemes for Diffusive Fluxes," Comput. Fluids, **101**, pp. 220–232.